



A parametric study of Io's thermophysical surface properties and subsequent numerical atmospheric simulations based on the best fit parameters

Andrew C. Walker^{a,*}, Chris H. Moore^c, David B. Goldstein^a, Philip L. Varghese^a, Laurence M. Trafton^b

^a Department of Aerospace Engineering, University of Texas, Austin, TX 78712, United States

^b Department of Astronomy, University of Texas, Austin, TX 78712, United States

^c Sandia National Laboratories, Albuquerque, NM 87185, United States

ARTICLE INFO

Article history:

Received 24 January 2012

Revised 1 May 2012

Accepted 1 May 2012

Available online 17 May 2012

Keywords:

Io
Atmospheres, Dynamics
Atmospheres, Structure
Jupiter, Satellites
Satellites, Atmospheres

ABSTRACT

Io's sublimation atmosphere is inextricably linked to the SO₂ surface frost temperature distribution which is poorly constrained by observations. We constrain Io's surface thermal distribution by a parametric study of its thermophysical properties in an attempt to better model the morphology of Io's sublimation atmosphere. Io's surface thermal distribution is represented by three thermal units: sulfur dioxide (SO₂) frosts/ices, non-frosts (probably sulfur allotropes and/or pyroclastic dusts), and hot spots. The hot spots included in our thermal model are static high temperature surfaces with areas and temperatures based on Keck infrared observations. Elsewhere, over frosts and non-frosts, our thermal model solves the one-dimensional heat conduction equation in depth into Io's surface and includes the effects of eclipse by Jupiter, radiation from Jupiter, and latent heat of sublimation and condensation. The best fit parameters for the SO₂ frost and non-frost units are found by using a least-squares method and fitting to observations of the Hubble Space Telescope's Space Telescope Imaging Spectrograph (HST STIS) mid- to near-UV reflectance spectra and Galileo PPR brightness temperature. The thermophysical parameters are the frost Bond albedo, α_F , and thermal inertia, Γ_F , as well as the non-frost surface Bond albedo, α_{NF} , and thermal inertia, Γ_{NF} . The best fit parameters are found to be $\alpha_F \approx 0.55 \pm 0.02$ and $\Gamma_F \approx 200 \pm 50 \text{ J m}^{-2} \text{ K}^{-1} \text{ s}^{-1/2}$ for the SO₂ frost surface and $\alpha_{NF} \approx 0.49 \pm 0.02$ and $\Gamma_{NF} \approx 20 \pm 10 \text{ J m}^{-2} \text{ K}^{-1} \text{ s}^{-1/2}$ for the non-frost surface.

These surface thermophysical parameters are then used as boundary conditions in global atmospheric simulations of Io's sublimation-driven atmosphere using the direct simulation Monte Carlo (DSMC) method. These simulations are unsteady, three-dimensional, parallelized across 360 processors, and include the following physical effects: inhomogeneous surface frosts, plasma heating, and a temperature-dependent residence time on the non-frost surface. The DSMC simulations show that the sub-jovian hemisphere is significantly affected by the daily solar eclipse. The simulated SO₂ surface frost temperature is found to drop only ~ 5 K during eclipse due to the high thermal inertia of SO₂ surface frosts but the SO₂ gas column density falls by a factor of 20 compared to the pre-eclipse column due to the exponential dependence of the SO₂ vapor pressure on the SO₂ surface frost temperature. Supersonic winds exist prior to eclipse but become subsonic during eclipse because the collapse of the atmosphere significantly decreases the day-to-night pressure gradient that drives the winds. Prior to eclipse, the supersonic winds condense on and near the cold nightside and form a highly non-equilibrium oblique shock near the dawn terminator. In eclipse, no shock exists since the gas is subsonic and the shock only reestablishes itself an hour or more after egress from eclipse. Furthermore, the excess gas that condenses on the non-frost surface during eclipse leads to an enhancement of the atmosphere near dawn. The dawn atmospheric enhancement drives winds that oppose those that are driven away from the peak pressure region above the warmest area of the SO₂ frost surface. These opposing winds meet and are collisional enough to form stagnation point flow.

The simulations are compared to Lyman- α observations in an attempt to explain the asymmetry between the dayside atmospheres of the anti-jovian and sub-jovian hemispheres. Lyman- α observations indicate that the anti-jovian hemisphere has higher column densities than the sub-jovian hemisphere and also has a larger latitudinal extent. A composite "average dayside atmosphere" is formed from a collisionless simulation of Io's atmosphere throughout an entire orbit. This composite "average dayside" atmosphere without the effect of global winds indicates that the sub-jovian hemisphere has lower average column densities than the anti-jovian hemisphere (with the strongest effect at the sub-jovian point) due primarily to the diurnally averaged effect of eclipse. This is in qualitative agreement with the

* Corresponding author.

E-mail address: andrew.walker@mail.utexas.edu (A.C. Walker).

sub-jovian/anti-jovian asymmetry in the Lyman- α observations which were alternatively explained by the bias of volcanic centers on the anti-jovian hemisphere. Lastly, the column densities in the simulated average dayside atmosphere agree with those inferred from Lyman- α observations despite the thermophysical parameters being constrained by mid- to near UV observations which show much higher instantaneous SO₂ gas column densities. This may resolve the apparent discrepancy between the lower “average dayside” column densities observed in the Lyman- α and the higher instantaneous column densities observed in the mid- to near UV.

© 2012 Elsevier Inc. All rights reserved.

1. Introduction

The predominant mechanism for supporting the observed atmosphere on Io has long been a subject of debate. The three mechanisms originally proposed were volcanic plumes, sublimation from SO₂ surface frosts, and sputtering from SO₂ surface frosts. Cheng and Johnson (1989) give a detailed review of sputtering models and also show that sputtering is a minor process in support of the dayside atmosphere since it can only produce an atmosphere limited to 10^{15} – 10^{16} cm⁻² and recent observations (Jessup et al., 2004; Feaga et al., 2009) show that large portions of the dayside exceed those limits. Therefore, sputtering is a secondary mechanism of atmospheric support except possibly near the poles and on the nightside (away from active volcanic plumes) where the vapor pressure of SO₂ is very low. Observations over the last 20 or more years have conflicted over the dominant process with a roughly 50/50 split between those observations that support a sublimation-driven atmosphere and those that support a volcanically-driven atmosphere. Recently, data on the disk-averaged spectra of the ν_2 band of SO₂ collected by Tsang et al. (2012) as a function of heliocentric distance have given strong evidence that there is a seasonal variation in the atmosphere that supports a sublimation-driven model; however, model fits to the observed data show that a substantial volcanic column is also needed. In this work, we hope to further constrain the column densities of gas from sublimation and volcanism.

As a first step, a parametric study of the thermophysical parameters of Io's surface is performed. The sublimation-driven atmosphere is most sensitive to the SO₂ surface frost temperature distribution due to the exponentially dependent SO₂ vapor pressure. Therefore, the thermophysical parameters of Io's surface must be well constrained to determine the correct column densities and morphology for the SO₂ sublimation atmosphere. There are numerous observations and thermal models of Io's surface which can help constrain the surface thermophysical parameters. Sinton and Kaminski (1988) observed Io in eclipse at several infrared wavelengths. To fit their data adequately they found that Io's surface must be composed of two different Bond albedo regimes (light and dark) and that the thermal inertia of the bright component was nearly 10 times that of the dark component. The bolometric Bond albedo is the true energy balance albedo and is dependent on all wavelengths. For the rest of this work, albedo will implicitly refer to Bond albedo for brevity. In their best fit two-albedo case having a dark component homogeneous in depth and a bright component inhomogeneous in depth (e.g. a thin layer of bright material over another material of differing thermal parameters), the albedos and thermal inertias were $\alpha_F = 0.475$ and $\Gamma_F = 56.65$ J m⁻² K⁻¹ s^{-1/2} for the thin layer of high albedo (bright) component and $\alpha_{NF} = 0.103$ and $\Gamma_{NF} = 5.17$ J m⁻² K⁻¹ s^{-1/2} for the low albedo (dark) component. Veeder et al. (1994) analyzed over 10 years of infrared observations of Io and constrained the global heat flow to be more than 2.5 W m⁻² with the majority coming from large warm (>200 K) volcanic regions. They fit the observational data with a thermal model comprised of three units: an equilibrium unit (zero thermal inertia, $\alpha_{NF} = 0.29$, ~20% areal

coverage of Io's entire surface), a reservoir unit (infinite thermal inertia, $\alpha_F = 0.58$ – 0.70 , ~80% areal coverage of Io's entire surface), and thermal anomalies (hot spots and thermal inertia anomalies).

Rathbun et al. (2004) analyzed Galileo photo-polarimeter radiometer (PPR) observations of Io's low temperature (<200 K) thermal radiation between 1999 and 2002. They observed the radiated flux and converted these measurements to brightness temperature (for single wavelength observations) or effective temperature (for open filter observations). The brightness temperature is defined as the temperature of a blackbody emitting an observed power at the observed wavelength whereas the effective temperature is defined as the temperature of a blackbody emitting an observed power at all wavelengths. To follow the convention of Rathbun et al. (2004), the calibrated temperatures will be referred to as “brightness temperatures” whether or not they are actual brightness temperatures or effective temperatures. See Table 1 of their paper for the filter used for each observation. They constrained the global heat flow to between 2.0 and 2.5 W m⁻² and also attempted to fit the surface thermal distribution with a two-component thermal model. The low-latitude diurnal variation is well matched by two components with the following thermophysical parameters: unit one ($\alpha_F = 0.70$, $\Gamma_F = 100$ J m⁻² K⁻¹ s^{-1/2}, 50% areal coverage) and unit two ($\alpha_{NF} = 0.34$, $\Gamma_{NF} = 40$ J m⁻² K⁻¹ s^{-1/2}, 50% areal coverage).

All of these observations require a minimum two-component surface thermal model to match the data. In all cases, one “bright” component has a fairly high albedo and a high thermal inertia. This “bright” component is likely associated with condensed patches of SO₂ surface frost; this component will be referred to as the “frost surface” for the rest of the paper. The second “dark” component has a lower albedo and thermal inertia. This “dark” component may be associated with either pyroclastic dusts or fine-grained sulfur allotropes; this component will be referred to as the “non-frost” surface for the rest of the paper. Although these observations agree on a two-component surface thermal model, the range of parameters which fit the data is surprisingly wide ($\alpha_F = 0.475$ – 0.70 , $\alpha_{NF} = 0.103$ – 0.34 , $\Gamma_F = 56.65$ J m⁻² K⁻¹ s^{-1/2} to $\sim\infty$, $\Gamma_{NF} = \sim 0$ – 40 J m⁻² K⁻¹ s^{-1/2}). One of the key goals of this paper is to further constrain these parameters based on recent observations.

Simonelli et al. (2001) used two sets of Galileo images taken with red, green, and violet filters to construct bolometric Bond albedo maps of Io's surface. Despite their observations being taken only over specific wavelength regimes, they were taken near the

Table 1
Thermophysical parameters for Io's surface from the literature.

Thermophysical parameters				Reference
Bond albedo		Thermal inertia		
α_F	α_{NF}	Γ_F	Γ_{NF}	
0.475	0.103	56.65	5.17	Sinton and Kaminski (1988)
0.58–0.70	0.29	∞	0	Veeder et al. (1994)
0.75	N/A	25–100	N/A	Kerton et al. (1996)
0.7	0.34	100	40	Rathbun et al. (2004)

maximum of the solar spectrum which increases the validity of the bolometric Bond albedo maps generated. Simonelli et al. (2001) found that the global mean bolometric Bond albedo was ~ 0.52 .

Some pure modeling of Io's surface thermal distribution has been done. Kerton et al. (1996) modeled Io's SO₂ surface frost thermal distribution including the effects of thermal inertia and albedo, latent heat, and a solid-state greenhouse effect. The solid state greenhouse effect allows for a porous surface where sunlight is able to penetrate deep into the surface layers. For SO₂ frost they chose $\alpha_f = 0.75$ and to define the thermal inertia they used parameters similar to those on other planetary bodies resulting in: $\Gamma_{\text{MIN}} \sim 25 \text{ J m}^{-2} \text{ K}^{-1} \text{ s}^{-1/2}$, $\Gamma_{\text{MAX}} \sim 100 \text{ J m}^{-2} \text{ K}^{-1} \text{ s}^{-1/2}$. They found that a high thermal inertia case tended to decrease the temperature near the subsolar point but increase temperatures near the edge of the disk and that the solid state greenhouse effect lowered the dayside surface temperatures everywhere ($\sim 5 \text{ K}$) while raising the subsurface solid temperatures.

There are other observations which can be used to constrain the surface thermophysical parameters. If the atmosphere is sublimation-dominated, then near the subsolar point (where there is small dynamic transport) the atmosphere will be in vapor pressure equilibrium with the surface. This assumption of vapor pressure equilibrium may break down on the morning portion of the dayside hemisphere where the atmosphere is enhanced by SO₂ desorbing from the non-frost surface (Walker et al., 2010). But the assumption is likely valid over the rest of the dayside hemisphere. Therefore, observed atmospheric column densities can be inverted to find the underlying surface frost temperature.

Jessup et al. (2004) observed the mid- to near-UV reflectance spectra of Io's anti-jovian hemisphere with HST STIS. They used their reflectance spectra data to infer SO₂ column densities at 22 points across the anti-jovian hemisphere. The SO₂ column densities in the latitude range 60°N–60°S peaked at $\sim 1.25 \times 10^{17} \text{ cm}^{-2}$ (with an additional $5 \times 10^{16} \text{ cm}^{-2}$ increase over Prometheus) and fell off smoothly away from the peak column density. At low latitudes ($< \pm 30^\circ$), the inferred column densities agree well with vapor pressure equilibrium (VPE) for a surface in radiative equilibrium with the insolation but depart from VPE further from the subsolar point. They concluded that the low latitude dayside atmosphere on the anti-jovian hemisphere is supported by sublimation from SO₂ surface frosts.

Feaga et al. (2009) analyzed an extensive set of Lyman- α observational data and were able to map the dayside SO₂ column density distribution by utilizing the reflected spectra from Io and the fact that SO₂ is a continuum absorber at Lyman- α wavelengths. The inferred dayside SO₂ column density distribution was found to be temporally stable with only small local changes, likely due to volcanic plumes. An asymmetry in the hemispheric column density was found between the anti-jovian and sub-jovian hemispheres with the anti-jovian hemisphere always having a more substantial column. Feaga et al. also found a distinct fall-off in the inferred SO₂ column density at mid-latitudes ($\sim 45^\circ$) that remains poorly understood. The DSMC simulated atmospheres are used to create an average dayside atmosphere which is compared to the Lyman- α observations in an attempt to give an alternative explanation for the observed anti-jovian/sub-jovian asymmetry (Feaga et al., 2009; Jessup et al., 2004; Moullet et al., 2008).

Walker et al. (2010) simulated Io's sublimation-driven atmosphere using an integrated thermal inertia model (Saur and Strobel, 2004) to compute the temperature distribution of the SO₂ frost and non-frost surfaces. They also analyzed two different residence time models. In conjunction with Gratiy et al. (2010), they found that a long residence time model for gas on the surface agreed better with the variation of 19.3 μm band depth with subsolar longitude from disk-averaged mid-infrared observations

(Spencer et al., 2005). However, the band depth profile as a function of subsolar longitude was shifted by $\sim 30^\circ$ due to the thermal lag between the subsolar point and the peak SO₂ frost temperature. Therefore, a more sophisticated thermal model has been incorporated into our DSMC code to determine whether such a large thermal lag should exist. The simulated atmosphere from Walker et al. (2010) was also compared to millimeter range observations (Moullet et al., 2008) that analyzed the Doppler shift in Io's atmosphere at eastern elongation and concluded that the observations were best fit by a super-rotating circumplanetary wind in the prograde direction. Although wind patterns in the simulated atmosphere of Walker et al. (2010) do not indicate a prograde super-rotating wind, the results agreed much better with Moullet et al. (2008) when the line broadening due to the circumplanetary winds was included. Lastly, Gratiy et al. (2010) used the simulated sublimation-driven atmosphere to compare to Lyman- α observations and found that the atmospheric morphology was quite different. Feaga et al. (2009) showed nearly barren poles and symmetric column densities along the equator from the dawn to dusk terminator; in contrast, Walker et al. (2010) found the atmosphere to be biased toward the dusk portion of the dayside hemisphere and did not find the observed fall-off in SO₂ gas column density at $\pm 45^\circ\text{N/S}$. The discrepancy between the simulated and observed atmospheric morphologies was thought to be due to the temperature distribution used in Walker et al. (2010).

In this paper, we will constrain the thermophysical properties of Io's surface by comparing to HST-STIS observations of inferred SO₂ column density (Jessup et al., 2004) and Galileo PPR observations of the surface brightness temperature (Rathbun et al., 2004). A brute force search utilizing a least squares error method is used to find the best fit thermophysical properties for the frost and non-frost surfaces. These best fit thermophysical properties are then used to generate frost and non-frost temperature distributions which serve as boundary conditions for a global atmospheric direct simulation Monte Carlo (DSMC) simulation. The resulting column densities, global winds, and thermal structure of the atmosphere are investigated immediately before Io enters eclipse.

2. Model

Io's surface thermophysical parameters will be constrained by a parametric study. The SO₂ surface frost thermophysical parameters are key to determining the morphology of the dayside atmosphere due to the exponential dependence of the vapor pressure on the surface frost temperature. The thermophysical parameters are constrained by using a least-squares error method and fitting to mid- to near-UV and Galileo PPR brightness temperature observations.

Using the best fit thermophysical parameters, Io's unsteady sublimation-driven atmosphere is then modeled using the DSMC method (Bird, 1994). The sublimation atmosphere ranges from collisional near the subsolar point to nearly free molecular near the poles and therefore a rarefied flow computational method such as DSMC is required to adequately capture the gas dynamics.

The surface thermal model is the primary improvement in this work compared to Walker et al. (2010) but the results seen in the overlying atmosphere are dramatic. In the sub-sections that follow, the improved surface model will first be presented followed by a discussion of the method used to find the best fit in the parametric study. Subsequently, a short summary of the DSMC method used in the global atmospheric simulations will be presented. The last four sub-sections of Section 2 present the specifics of the domain and parallelization for our DSMC gas dynamic simulations, the physical effects included in those simulations, hot spots, and the process whereby we achieve a quasi-steady state.

2.1. Thermal model of Io's solid surface

The SO₂ surface frost and non-frost temperatures are determined by solving the one-dimensional heat conduction equation with their respective thermal parameters

$$\rho c \frac{\partial T(\theta, \phi, z, t)}{\partial t} = \frac{\partial}{\partial z} \left[k \frac{\partial T(\theta, \phi, z, t)}{\partial z} \right] \quad (1)$$

where ρ is the density, c is the specific heat, k is the thermal conductivity, t is time, z is the depth into the surface, θ is the co-latitude, ϕ is the longitude, and T is the solid temperature (of frost or non-frost). The parameters ρ , c , and k (if independent of z) can be grouped together to a single thermal parameter known as the thermal inertia, Γ . The boundary conditions at the upper surface ($z = 0$) and at a depth where there are no diurnal changes ($z = d$) are given, respectively, by:

$$k \frac{\partial T(\theta, \phi, z, t)}{\partial z} \Big|_{z=0} = \varepsilon \sigma T^4(\theta, \phi, z = 0, t) - (1 - \alpha)(F_S(\theta, \phi, t) + F_J(\theta, \phi)) - q_{SUB}(\theta, \phi, t) + q_{COND}(\theta, \phi, t) \quad (2a)$$

$$k \frac{\partial T(\theta, \phi, z, t)}{\partial z} \Big|_{z=d} = Q_T \quad (2b)$$

$$F_S = F_{S-MAX} \sin(\theta) \cos(\phi + \omega t) \quad (2c)$$

$$F_J = F_{J-MAX} \sin(\theta) \cos(\phi) \quad (2d)$$

where ε is the emissivity, σ is the Stefan–Boltzmann constant, α is the albedo, F_S is the solar flux, F_J is the flux of radiation from Jupiter, q_{SUB} and q_{COND} are the heating terms due to the latent heat of sublimation and condensation, respectively, F_{S-MAX} is the maximum solar flux, ω is the planetary angular rotation rate, F_{J-MAX} is the maximum Jupiter flux, and Q_T is the endogenic heating of the passive background and does not include the additional heating from hot spots. Note that F_S is zero past the terminator on the nightside and F_J is zero on the anti-jovian hemisphere. The total endogenic heating rate will be the sum of the passive background and hot spot endogenic heating rates. $Q_T = 1.0 \text{ W m}^{-2}$ will be used in this work as modeling of Galileo PPR observations showed that it fits the data best (Rathbun et al., 2004). The total endogenic heating rate is well constrained to be $\sim 2.5 \text{ W m}^{-2}$ and our simulations are consistent with this total endogenic heating rate by emitting $\sim 1.0 \text{ W m}^{-2}$ from the passive background and $\sim 1.5 \text{ W m}^{-2}$ from the hot spots. The heating rate from hot spots is calculated by integrating the emitted flux from all hot spots and then dividing by the Io's surface area (Marchis et al., 2005). F_{S-MAX} is chosen to best match the thermal fit by Rathbun et al. (2004) using the same thermal parameters as their inhomogeneous model. Their thermal profile was fit to Galileo orbits I24 (October 10, 1999), I25 (November 25, 1999), I27 (February 22, 2000), I31 (August 5, 2001), I32 (October 15, 2002), and I33 (January 17, 2003). The heliocentric distance and resulting solar flux for each Galileo orbit that were used are listed in Table 2. The solar flux varies by approximately 15% between the cases where Io is closest and furthest from the Sun but the effect of this solar flux variation is not clearly seen in Fig. 7 of Rathbun et al. (2004). The best fit F_{S-MAX} is found to be 54.6 W m^{-2} and corresponds approximately to a date in late 2000.

The emissivity, ε , is assumed to be unity (Rathbun et al., 2004). We neglect heating of the surface by plasma impact since our plasma energy flux (1.3 mW m^{-2} ; Linker et al., 1991) is negligible compared to the other heating terms such as endogenic heating which is $\sim 10^3$ times greater over the entire surface. The Γ and α values for the frost and non-frost surfaces are found through a parametric study discussed in Section 2.2. The other important parameters related to the thermal model are summarized in Table 3.

Table 2

The date, heliocentric distance, solar flux, and variation from the chosen solar flux value for each of the Galileo orbits used for the determination of the best fit parameters.

Orbit name	Date	Io distance from Sun (AU)	Solar flux (W m^{-2})	% Variation from chosen value
I24	10–October–99	4.96	55.92	+2.42
I25	25–November–99	4.96	55.82	+2.24
I27	22–February–00	4.98	55.50	+1.65
I31	5–August–01	5.11	52.53	–3.79
I32	15–October–02	5.27	49.51	–9.32
I33	17–January–03	5.31	48.73	–10.75

Table 3

The fixed parameters in the thermal model.

Parameter	Value
Emissivity, ε	1
Best fit solar flux, F_S	54.6 W m^{-2}
Jupiter blackbody temperature, T_{JUP}	130 K
Passive background endogenic heat flux	1.0 W m^{-2}
Eclipse duration	2 h
Ingress/egress duration for Io disk	3 min

Io is tidally locked and therefore only the sub-jovian hemisphere sees the radiated flux from Jupiter. In addition, Io's sub-jovian hemisphere experiences a solar eclipse for ~ 2 h during each rotation. The eclipse model resolves the timescale of ingress and egress; Jupiter's shadow is realistically swept across Io's disk over the ~ 3 min of ingress and egress corresponding to Io's disk being in Jupiter's penumbra. Both of these effects are incorporated in the surface thermal model. The blackbody radiation from Jupiter uses $T_{JUP} = 130 \text{ K}$ and therefore the "Jupiter heating" is a relatively small but steady heating term ($\sim 0.67 \text{ W m}^{-2}$ at the sub-jovian point); however, eclipse by Jupiter has a large effect on the global surface thermal distribution. The sub-jovian hemisphere will see 2 h less sunlight per day than the anti-jovian hemisphere; therefore, the sub-jovian hemisphere will be relatively cooler than the anti-jovian hemisphere. The steady shine of Jupiter flux is not enough to make up for the sunlight lost by the sub-jovian hemisphere during eclipse (see Section 3.1.3). This will be shown in the following sections to have important implications for the sub-jovian/anti-jovian hemisphere asymmetry observed in the mid-infrared (Spencer et al., 2005), Lyman- α (Feaga et al., 2009), and millimeter range (Moulet et al., 2008) where the sub-jovian hemisphere consistently has lower column densities than the anti-jovian hemisphere. Latent heat effects due to sublimation and condensation of SO₂ gas molecules are also treated, but it will be shown *a posteriori* that they have negligible impact on the surface temperature. Radiative exchange between the surface and the atmosphere is neglected; this may be a poor assumption and will be the subject of future work.

The thermal model is discretized following the method outlined in Spencer et al. (1989). Following their parameterization, z is replaced with $\zeta = z/l_s$, where $l_s = \sqrt{(k/\rho c \omega)}$ is the skin depth (between about 10 cm and 1 m depending on the thermal conductivity). This reduces Eqs. 1, 2a, and 2b to

$$\frac{\partial T(\theta, \phi, \zeta, t)}{\partial t} = \omega \frac{\partial^2 T(\theta, \phi, \zeta, t)}{\partial \zeta^2} \quad (3a)$$

$$\begin{aligned} \sqrt{\omega} \Gamma \frac{\partial T(\theta, \phi, \zeta, t)}{\partial \zeta} \Big|_{\zeta=0} &= \varepsilon \sigma T^4(\theta, \phi, \zeta = 0, t) \\ &\quad - (1 - \alpha)(F_S(\theta, \phi, t) + F_J(\theta, \phi)) \\ &\quad - q_{SUB}(\theta, \phi, t) + q_{COND}(\theta, \phi, t) \end{aligned} \quad (3b)$$

$$\left. \frac{\partial T(\theta, \phi, \zeta, t)}{\partial \zeta} \right|_{\zeta=1} = \frac{Q_T}{\Gamma \sqrt{\omega}} \quad (3c)$$

We forego the additional scaling of the temperature by the subsolar equilibrium temperature as described by Spencer et al. (1989). The discrete equivalents of Eqs. (3a)–(3c) after solving for the quantities of interest are

$$T_i^{n+1} = T_i^n + \frac{\omega \Delta t}{\Delta \zeta^2} (T_{i+1}^n - 2T_i^n + T_{i-1}^n) \quad (4a)$$

$$T_0^{n+1} = T_0^n + 2 \frac{\omega \Delta t}{\Delta \zeta^2} (T_1^n - T_0^n) - \frac{2\sqrt{\omega} \Delta t}{\Gamma \Delta \zeta} (\varepsilon \sigma T_0^{n4} - (1 - \alpha)(F_S + F_J) - q_{SUB} + q_{COND}) \quad (4b)$$

$$T_{N-1}^{n+1} = T_{N-1}^n + 2 \frac{\omega \Delta t}{\Delta \zeta^2} (T_{N-2}^n - T_{N-1}^n) + \frac{Q_T \Delta \zeta}{\Gamma \sqrt{\omega}} \quad (4c)$$

These equations are second order central difference in space and first order forward difference in time. N is the number of slabs in depth and $\Delta \zeta$ is the thickness of each slab. The values for $N=32$ and $\Delta \zeta=0.25$ were taken from Spencer et al. (1989) but were also independently tested for convergence. The fraction of frost and non-frost (discussed in detail in Section 2.5) present at the surface are assumed to be uniform in depth. Io's rotation was discretized with a timestep $\Delta t=100$ s and this too was tested for (timestep) convergence (the timestep is reduced to 0.5 s when modeling the full atmosphere to resolve the mean time between collisions). These equations apply to both the frost and non-frost surfaces where T , α , and Γ are the respective parameters of that surface type.

2.2. Parametric study of thermophysical parameters

In the fitting process, the frost albedo is allowed to vary between 0.45 and 1.0; however, frost albedos below 0.55 are assumed unphysical based on correlations between regions of moderately high Bond albedos observed by Simonelli et al. (2001) and regions of high frost fraction (Douté et al., 2001) that set a physical limit on the minimum SO₂ frost Bond albedo at 0.55 (Tsang et al., 2012). The non-frost albedo is thus fixed once the frost albedo has been determined as Io's global mean albedo is well constrained to be ~ 0.52 (Simonelli et al., 2001) and therefore the SO₂ frost and non-frost albedos weighted by their average areal coverage must give the mean global albedo. The frost and non-frost thermal inertias are allowed to vary between 0 and (although in practice the upper limit was placed at $10,000 \text{ J m}^{-2} \text{ K}^{-1} \text{ s}^{-1/2}$, a value large enough to easily contain the best fit parameters).

In step (i) of the fitting process, mid- to near-UV observations of the anti-jovian hemisphere column density (Jessup et al., 2004) are used to infer SO₂ surface frost temperatures assuming vapor pressure equilibrium and a surface uniformly covered by SO₂ surface frosts starting from Eq. (5)

$$N_{OBS} = \frac{P_{VAP}}{m_{SO_2} g} \quad (5)$$

where N_{OBS} is the observed SO₂ column density (Jessup et al., 2004), m_{SO_2} is the molecular mass of SO₂, g is the gravitational acceleration at Io's surface, and P_{VAP} is the vapor pressure of SO₂ (in Pascals) defined by the Clausius–Clapeyron equation

$$P_{VAP} = Ae^{-B/T_F} \quad (6)$$

Here $A=1.52 \times 10^{13}$ Pa, $B=4510$ K, and T_F is the SO₂ surface frost temperature (Wagman, 1979). Substituting for Eq. (6) into Eq. (5) and then solving for T_F yields

$$N_{OBS} \frac{Ae^{-B/T_F}}{m_{SO_2} g} \rightarrow T_F = \frac{B}{\ln(A/(N_{OBS} m_{SO_2} g))} \quad (7)$$

Note that the assumption of VPE only holds when the atmosphere is dominated by sublimation rather than desorption from the non-frost surface (which occurs over portion of the morning dayside atmosphere), there is no net transport of mass, there is no sputtering from SO₂ surface frosts, and there are no chemical reactions (Moore, 2011). When the atmosphere departs substantially from VPE (>20%), a VPE correction factor, β , must be applied to the T_F inferred from mid- to near UV observations (Jessup et al., 2004). The details of how β is calculated and applied are described in step (iv).

In step (ii), a brute force search through frost albedos and thermal inertias is performed with the thermal model described in Section 2.1 simulating T_F for each combination of α_F and Γ_F . The simulated and inferred T_F are compared at the locations listed in Table 2 of Jessup et al. (2004) and the quality of the fit for that particular combination of thermophysical parameters is computed based on a least-squares error method in which each data point is given equal weight.

In Step (iii), a brute force search through Γ_{NF} is performed with the frost thermophysical parameters fixed as the best fit parameters from step (ii). For each Γ_{NF} , the simulated brightness temperature distribution, T_B , is calculated by summing the radiated flux from the frost and non-frost surface areas in a given surface cell and finding the equivalent blackbody temperature. The observed T_B distributions, to which the simulated T_B distributions are compared, were taken at several different subsolar longitudes but then combined as a function of time of day (Rathbun et al., 2004). The underlying frost fraction for each observation was undoubtedly different and therefore, the frost fraction is assumed uniform (50% frost/50% non-frost) for the calculation of the simulated T_B distribution since the mean frost fraction is near 50% (Walker et al., 2010). The simulated and observed T_B distributions (Rathbun et al., 2004) are then compared and a best non-frost Γ_{NF} is found via a least-squares error method where each point is given equal weight. Thus, both the frost and non-frost thermophysical parameters are constrained before iterating to correct for the initial assumption of VPE.

In step (iv), the errors generated from the initial assumption of VPE are corrected by computing and applying the VPE correction factor, β , to the inferred T_F . Fig. 1 shows the percent difference between the atmospheric SO₂ column density in VPE with modeled T_F and the actual SO₂ column density computed in subsequent DSMC simulations of the atmosphere using the best fit thermophysical parameters after completing steps (i)–(iii). Note that the DSMC simulated atmosphere used for this comparison does not include the effect of intermolecular collisions because it would be prohibitively expensive in terms of computation time. To calculate β (at a central longitude of 180°W), the percent difference is computed at each of the locations observed by Jessup et al. (2004) where the percent difference is

$$\beta = 100 \frac{N_{DSMC} - N_{VPE}}{N_{VPE}} \quad (8)$$

In Fig. 1, the departure from VPE is small (<10%) near noon and on the dusk portion of the disk but large (>100%) on the morning portion of the disk because the quick thermal response of the non-frost surface at dawn leads to rapid desorption of SO₂ molecules from the non-frost surface. This atmospheric enhancement near dawn was discussed in Walker et al. (2010) and termed the “dawn atmospheric enhancement” or DAE. Departures from VPE due to transport of mass by circumplanetary winds are minor and dwarfed by the desorption of SO₂ from the non-frost surface (Walker et al., 2010). Although not included in the current model, sputtering and chemical reactions can also lead to departures from

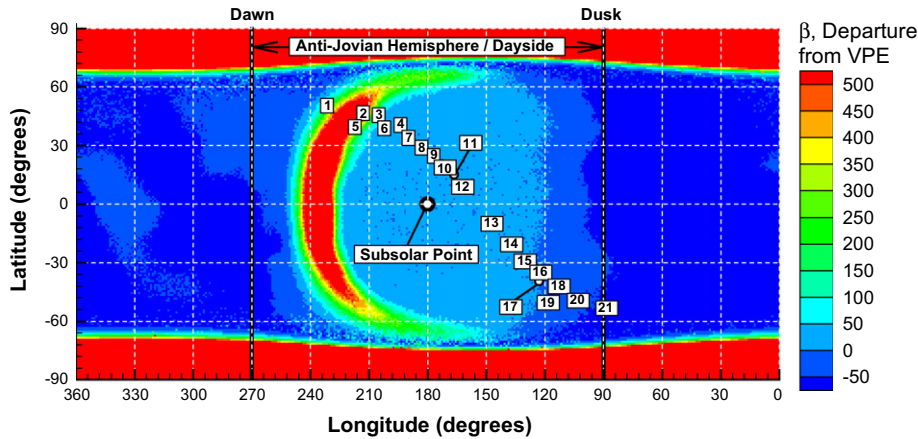


Fig. 1. The percent difference as a function of latitude and longitude between the analytic atmospheric SO_2 column density based on equilibrium with the surface frost temperature and the column computed in the DSMC simulation with best fit parameters. The central (subsolar) longitude is located at the anti-jovian point (180°W). The red regions near the poles are areas in the DSMC simulations with no molecules. Squares represent the mean location of the mid- to near-UV observations. See Fig. 2 in Jessup et al. (2004) for the areal coverage of each bin number. Note that bin 13 from Jessup et al. (2004) has been removed because of the large volcanic contribution of Prometheus; therefore, bin notations in the present work above 12 are offset by 1 compared to their data. (For interpretation of the references to color in this figure legend, the reader is referred to the web version of this article.)

VPE (Moore, 2011). Due to the DAE, the original assumption of VPE breaks down near the dawn terminator and β must be applied to the surface frost temperatures (Jessup et al., 2004) that are being fit.

The areas near the poles exhibit large variations from VPE because the statistics in the DSMC simulation break down there; however the mid- to near-UV data used for the least squares fitting does not extend to these regions. There are no molecules near the poles due to the constant weight (used in the DSMC simulations) near the poles and the continuously dropping P_{VAP} with latitude. Unfortunately, the simulations require a constant weight near the poles because the equilibrium P_{VAP} drops so precipitously near the poles ($\sim 10^{12}$ times lower at 70 K compared to the subsolar P_{VAP} at ~ 120 K). Computational errors from massive cloning and destruction of molecules arise (even when the gas is collisionless) when the weight is allowed to adapt freely and balance the number of computational SO_2 molecules in each column of cells. See Bird (1994) for a detailed discussion of cloning and destroying molecules which move between computational cells having different cell weights.

β , calculated in Eq. (8), is applied to the mid- to near-UV inferred column densities (Jessup et al., 2004) as shown in the following equation:

$$N_{CORR} = \frac{N_{OBS}}{(1 + \beta)} \rightarrow T_F = \frac{4510 \text{ K}}{\ln(1.52 \times 10^{13} / N_{CORR} m_{\text{SO}_2} g)} \quad (9)$$

This yields “corrected” VPE column densities, N_{CORR} , which can be inverted to find the “corrected” T_F that will be used for the next iteration of the fitting process (steps (ii) and (iii)). Steps (ii)–(iv) are then repeated while matching instead to the “corrected” T_F computed via Eq. (9). The correction process is iterated until the thermophysical parameters converge to within 5%. Fig. 2 shows a flow chart for the logic used in the parametric study.

2.3. DSMC method

The DSMC method (Bird, 1994) is a particle-based scheme that models a relatively small number of particles (which represent a far larger number of actual particles), and then moves and collides those molecules in a cell-discretized domain. Movement and collisions between particles are decoupled by the dilute gas approximation because the time spent in collisions is much less

than the time spent between collisions and by using a time step smaller than the mean collision time. DSMC can accurately model gas dynamics where the mean free path becomes comparable to a characteristic flow length scale; a situation where Navier–Stokes continuum solvers will break down. The collision model used is a variable hard sphere (VHS) model with the parameters for SO_2 . The macroscopic properties of interest (number density, translational temperature, bulk velocity, etc.) are computed by sampling the molecules in each cell. In the next few sections (Sections 2.4–2.7), we will highlight some of the changes made to the simulation process since the previous work by Walker et al. (2010).

2.4. Domain and parallelization

The DSMC code utilized is both three-dimensional and parallel. The DSMC code uses a MPI parallel implementation with the domain decomposed between 360 processors in both latitude and longitude. Each processor simulates 10° of longitude and 18° of latitude. The domain spans all latitudes and longitudes with 1° resolution and from Io’s surface up to 1400 km above Io’s surface with the upper boundary is treated as a vacuum. The vertical domain is broken into two sections with an altitude 400 km above the surface as the interface between the two sections. Below 400 km, the DSMC method is employed (i.e. the effect of collisions is computed) with 400 vertical cells. Above 400 km, a “free molecular cell” is used in which the gas is treated as free molecular (i.e. without collisions). The “free molecular cell” is a single cell which spans from 400 km to 1400 km above the surface and is used to reduce unphysical escape from the top of the domain. With a 1400 km top, only molecules which have a velocity greater than 65% of escape velocity will escape the top of the “free molecular cell”. Estimating the peak surface temperature to be ~ 120 K and assuming a Maxwellian speed distribution, this corresponds to the tail of the speed distribution with fewer than 0.001% of molecules possessing speeds greater than 65% escape velocity. The lower surface of the domain (Io’s surface) has a unit sticking coefficient.

The vertical grid below 400 km is resolved by 400 cells using five adaptable “linear segments” with 20% of the total gas column density in each “linear segment”. In each “linear segment”, the cell sizes are computed based on the local gas properties at the segment endpoints and the cell sizes vary linearly between those

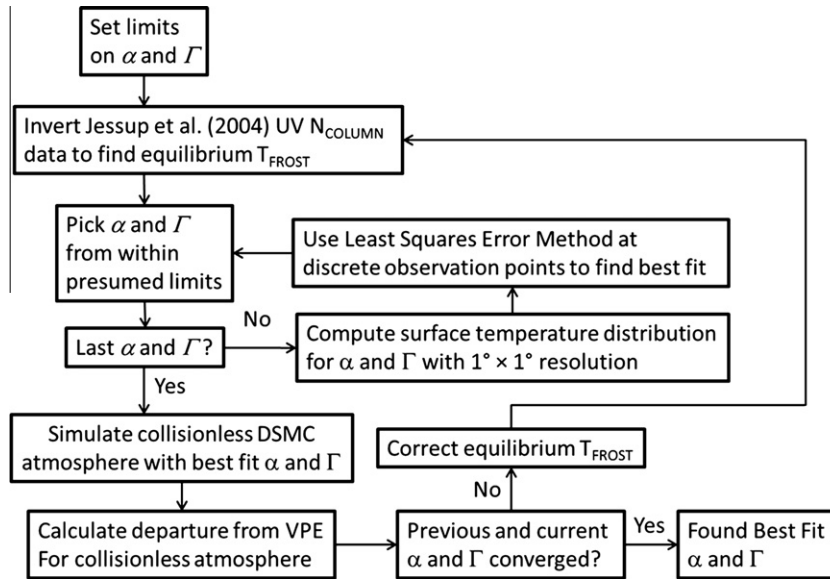


Fig. 2. A flowchart detailing the logic chain in the parametric study.

endpoints. Initially, the grid starts with uniform 1 km cells and then the local gas properties are sampled for 750 time steps. Based on the sampled local gas properties the “linear segments” and their cell sizes are adapted each consecutive 750 timesteps. The linearly segmented adaptive grid stretching is used in place of an exponentially stretched grid for computational efficiency because linear segments allow for the indices of a molecule to be calculated analytically whereas the exponentially stretched grid required a searching technique. The “linear segments” grid stretching method allows for each column of cells to have a different vertical grid stretching which can make visualization quite difficult and therefore a separate uniform output grid is used to analyze the data. The output grid uses the same resolution in latitude and longitude but uses uniform 1 km vertical resolution. See Moore (2011) and Moore et al. (2012) for details on the “linear segments” grid stretching method.

2.5. Physical effects

The DSMC code used to simulate the sublimation atmosphere includes many physical effects which are important to the atmospheric dynamics. A brief summary of each effect is given here but the reader should refer to Walker et al. (2010, Sections 3.1–3.6 and 3.8) for a more detailed explanation. Note that the thermal model described in Section 3.3 of Walker et al. (2010) has been supplanted by the model detailed in Section 2.1 of this paper.

The patchy nature of Io’s SO₂ surface frost (see Fig. 3) is modeled based upon Galileo NIMS observations (Douté et al., 2001). They observed the SO₂ surface frost fraction distribution, f , over approximately 75% of Io’s surface with 1° resolution. In this work, unobserved longitudes between ~0° and 60° are linearly interpolated, while unobserved high latitudes are interpolated by hand. The frost and non-frost components are assumed segregated (on a sub-cell scale) with the relative percentages of frost and non-frost given by f and $(1 - f)$, respectively.

The SO₂ surface frost is assumed to sublimate based on the vapor pressure equilibrium. The number flux of SO₂ molecules sublimated is then defined by

$$N_{SUB} = \frac{P_{VAP}}{\sqrt{2\pi k_B T_F M_{SO_2}}} \cdot f \quad (10)$$

where k_B is the Boltzmann constant. If an SO₂ molecule hits the non-frost surface, it will stick for a residence time determined by the non-frost surface temperature, T_{NF} . The residence time on the non-frost surface is given by (Sandford and Allamandola, 1993):

$$t_{res} = \frac{e^{\Delta H_S/k_B T_S}}{v_0} \quad (11)$$

where ΔH_S is the binding energy of the surface matrix site ($\Delta H_S/k_B = 3460 \pm 40$ K) and $v_0 = 2.4 \times 10^{-12} \text{ s}^{-1}$ is the lattice vibrational frequency of SO₂. ΔH_S and v_0 assume that the non-frost surface is coated with an optically thin film of SO₂ molecules; however, the film is assumed thin enough not to affect the thermophysical properties of the non-frost solid. To fit the disk-averaged mid-infrared spectra, a “long” residence time (Walker et al., 2010) is used (which increases the residence time of Eq. (11) by a factor of 1000). The “long” residence time model likely models the high porosity of the non-frost surface where molecules get trapped for many bounces. In future work, a more rigorous parametric study of the surface interaction constants, ΔH_S and v_0 , will be performed.

Io’s atmosphere is heated by the bombardment of ions from the jovian plasma torus. This heating is assumed to enter radially from the top of the domain and is absorbed by the gas, dependent on the gas density. The plasma energy flux absorbed by the gas is deposited equally into the translational and rotational degrees of freedom assuming local equilibrium. Plasma energy is not directly input to the vibrational degrees of freedom for lack of an adequate method; however, the plasma energy will be indirectly transferred into vibration via collisions between SO₂ molecules that have absorbed translational or rotational energy. The plasma energy flux is assumed to be ~1.3 mW m⁻² based on the fraction of plasma energy that reaches the exobase (Linker et al., 1988; Pospieszalska and Johnson, 1996; Austin and Goldstein, 2000). For a detailed description of the plasma model see Austin and Goldstein (2000).

2.6. Hot spots

Keck AO infrared observations (Marchis et al., 2005) provide the basis to model 26 persistent hot spots on Io’s surface. Each hot spot is assumed to be a circular disk on the surface with a temperature, area, and position (latitude and longitude to the nearest degree) taken from Tables 3 and 5a–5c of Marchis et al. (2005). SO₂

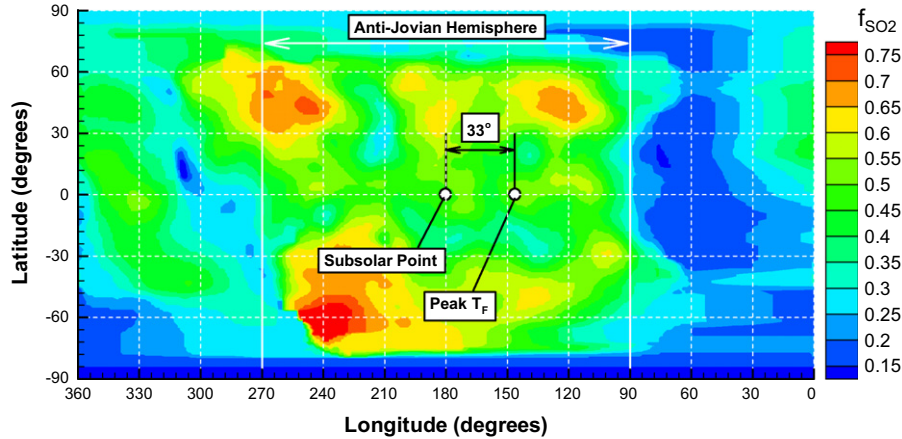


Fig. 3. Frost fraction as a function of latitude and longitude (Douté et al., 2001). High latitudes are interpolated by hand while longitudes between $\sim 0^\circ$ and 60° are linearly interpolated.

molecules which land on the hot spot surface thermally equilibrate with the surface and then desorb instantaneously. The area covered by hot spots is assumed not to sublimate (as any SO_2 surface frost would vaporize rapidly at the hot spot temperature) and there is zero net mass flux from the hot spots (i.e. we do not model any plumes from these hot spots). For more detail on hot spots, see Walker et al. (2011). Table 4 shows the temperature, areas, and positions of the 26 hot spots.

2.7. Approaching a quasi-steady state

Simulation of Io's atmosphere is technically an unsteady and nearly periodic problem; however, Io's rotation is fairly slow in comparison to the other (modeled) time scales that affect the atmosphere and therefore the gas dynamic simulations do reach a quasi-steady state. There are a variety of different time scales that affect the approach to quasi-steady state. The approach to

steady state is broken down into several sequential steps. Note that the following steps are not connected with those described in Section 2.2.

In step (i), the first (and longest) time scale present in our simulations – the approach of the surface temperature distribution to a periodic steady state – is computed. The thermal model (Eq. (4)) must converge on a “deep temperature”, T_{DEEP} , which is the temperature at the lower boundary of the one-dimensional domain (e.g. several meters below the solid surface of Io). The frost and non-frost surfaces are allowed to have independent values of T_{DEEP} . An arbitrary temperature (120 K) is initially defined for the temperature of the entire domain and then T_{DEEP} at a particular latitude and longitude is computed by averaging the temperature of that point throughout an entire day (e.g. the diurnal average). The updated T_{DEEP} is then assigned and the process is iterated through several Io rotations until T_{DEEP} converges to within 10^{-3} K. This relaxation process is computed uncoupled from the atmosphere and therefore the latent heats of sublimation and condensation are not included. To include the latent heats of sublimation and condensation and couple the atmosphere to the surface thermal model would be computationally prohibitive (increasing the computational time by several orders of magnitude); however, as will be shown later the effect of latent heat is relatively minor.

In step (ii), the second longest time scale – the approach of the number of SO_2 molecules stuck to the non-frost surface to a periodic steady state – is computed. The non-frost surface is initially assumed to be barren of any SO_2 . Molecules are introduced by creating them at the frost surface assuming VPE with the periodic T_F discussed in step (i). The atmosphere is assumed to be collisionless for step (ii) with a relatively low number of representative molecules ($\sim 180,000$ per processor or 1000 per column of cells). This free molecular atmosphere is then computed for three full Io rotations with a 10 s time step (small enough to adequately resolve the ballistic trajectories of SO_2 molecules). The non-frost surface boundary condition is deemed quasi-steady state when the two subsequent rotations are seen to be periodic when viewing the same subsolar longitude. In practice, this occurs after the 3rd rotation.

In step (iii), once the lower surface boundary conditions have reached a quasi-steady state, the global atmosphere, including intermolecular collisions, can be computed. The relatively low number of molecules used in step (ii) is increased by a factor of 10 by cloning each molecule, and the time step is decreased to 0.5 s. This time step is adequate to resolve the mean time between collisions in all but the densest regions of the atmosphere. Then

Table 4

The name, co-latitude, longitude, area, and surface temperature of 26 persistent hot spots observed by Marchis et al. (2005).

Name	Longitude	Co-latitude	Area (km ²)	Temperature (K)
Surt	337	49	68	458
Fuchi	328	65	2222	285
Sengen	314	122	15	492
Loki	308	80	10,875	332
Dazhbog	302	37	5166	338
Hephaestus	289	90	531	331
Ulgen	288	132	502	368
Unnamed	281	41	11	568
Daedalus	274	70	572	360
Pele	257	110	37	566
Pillan	244	104	674	363
Isum	209	62	141	387
Marduk	209	117	132	428
Zamama	174	73	42	414
Culann	165	111	348	338
Prometheus	156	94	644	335
Tupan	142	112	95	378
Malik-Thor	135	54	236	433
Amirani	115	70	334	366
Unnamed	93	129	931	358
Gish Bar	91	76	1116	350
Zal	79	64	158	376
Tawhaki	77	90	797	375
Masubi	56	135	204	426
Janus	39	97	27	559
Uta	22	127	71	432

cloned molecules are randomized through collisions and surface interactions for approximately 500 s. Walker et al. (2010) found that quasi-steady state circumplanetary flow developed after about 4 h: the time it takes for the pressure driven winds to develop after intermolecular collisions are turned on. We use the same time scale here and time-average over the last few hundred time steps to improve statistics.

3. Results

3.1. Thermophysical parametric study

Using the method outlined in Section 2.2, the best fit thermo-physical parameters for the frost and then the non-frost surfaces are computed. The best fit parameters are found to be $\alpha_F \approx 0.55 \pm 0.02$ and $\Gamma_F \approx 200 \pm 50 \text{ J m}^{-2} \text{ K}^{-1} \text{ s}^{-1/2}$ for the SO_2 frost surface and $\alpha_{NF} \approx 0.49 \pm 0.02$ and $\Gamma_{NF} \approx 20 \pm 10 \text{ J m}^{-2} \text{ K}^{-1} \text{ s}^{-1/2}$ for the non-frost surface. Converging to the best fit parameters (Section 2.2) required three steps to converge to within 5% of the previous values for the thermophysical parameters of interest. Error estimates represent the range of parameters within 10% of the best fit χ^2 . Sections 3.1.1 and 3.1.2 discuss the SO_2 frost and non-frost surface temperatures for a subsolar longitude of 180°W .

3.1.1. Frost best fit parameters

As discussed in Section 2.2, the constraint $\alpha_F > 0.55$ (Tsang et al., 2012) is applied based on correlations between regions of high mean albedo (Simonelli et al., 2001) and high frost fraction (Douté et al., 2001). Lower albedos with higher thermal inertias are found to give better fits by allowing a higher peak temperature and with little fall off in longitude (or time of day); however, these violate the $\alpha_F > 0.55$ assumption. Fig. 4a shows the best (but unphysical) fit occurring in the lower right hand corner at $\alpha_F \sim 0.50$ and $\Gamma_F \sim 300 \text{ J m}^{-2} \text{ K}^{-1} \text{ s}^{-1/2}$. If the domain is extended to even lower albedos and higher thermal inertias, the best fit lies at $\alpha_F \sim 0.46$ and $\Gamma_F \sim 1000 \text{ J m}^{-2} \text{ K}^{-1} \text{ s}^{-1/2}$; however, these parameters were deemed unphysical due to the unreasonably low frost albedos (< 0.55). If the restriction of $\alpha_F > 0.55$ was ignored, then the best fit thermophysical parameters would yield an SO_2 surface temperature distribution with less diurnal variation ($< 5 \text{ K}$ change between high noon and midnight) and a 1–2 K higher diurnally averaged temperature (due to the lower α_F).

The simulated T_F using the best fit parameters is plotted in Fig. 4b along with the observational data (Jessup et al., 2004). The best fit slightly overestimates the peak but generally agrees at large bin numbers (the afternoon region of the surface) except at the edges (bin numbers near 0 and 20). The agreement is worse at small bin numbers (the morning portion of the surface) where the observations become noisy and have little drop-off with solar zenith angle. Simulations of Io's atmosphere above a simplified surface model have recently been performed that include plasma chemistry and sputtering due to energetic ions (Moore, 2011; Moore et al., 2012). These simulations find that sputtering becomes significant when the surface temperature drops below $\sim 108 \text{ K}$. It may be that the lack of drop-off in inferred T_F near the dawn terminator is due to sputtering which is not included in our numerical model presented here. Sputtering would likely keep the column density fairly constant below $\sim 108 \text{ K}$ and reduce the discrepancy between the simulated best fit and observed T_F in bins 1–5.

The relatively high thermal inertia we find for the frost indicates the presence of at least partially annealed or coarse-grained ice. A process for annealing SO_2 frost on Io was suggested by Sandford and Allamandola (1993) as a result of the large diurnal temperature change for an initially porous low thermal inertia frost. Initially porous SO_2 frost on the surface originating from either

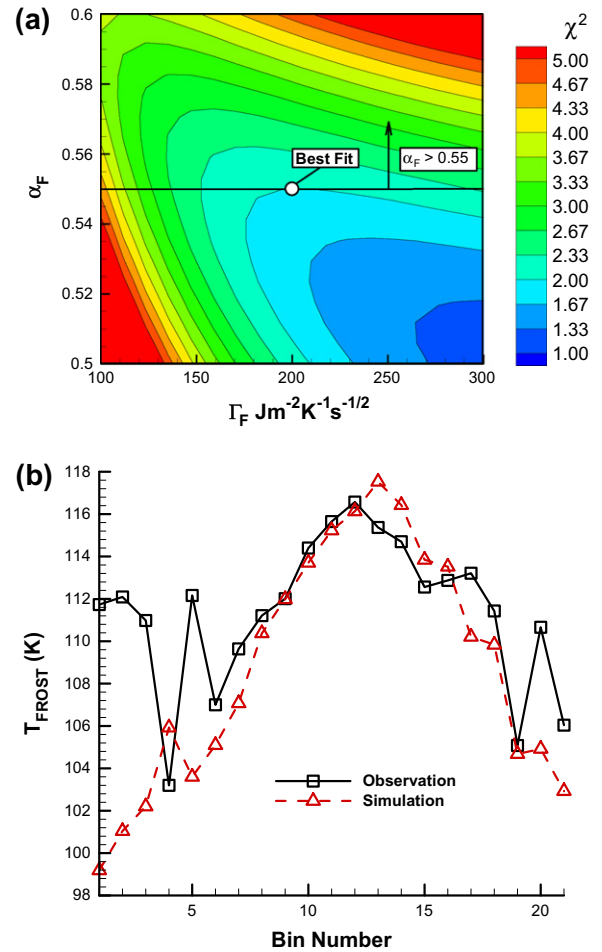


Fig. 4. (a) χ^2 (least squared error) as a function of frost albedo, α_F , and thermal inertia, Γ_F . The range of α_F extends to 0.50 to emphasize that better fits exist at lower albedos. When the best fit is restricted to an $\alpha_F > 0.55$ it is found at $\Gamma_F \sim 200 \text{ J m}^{-2} \text{ K}^{-1} \text{ s}^{-1/2}$ and $\alpha_F \sim 0.55$ for the final iteration. (b) A comparison of the observationally inferred (Jessup et al., 2004) and simulated surface frost temperatures (with the best fit thermophysical parameters) at the locations (bin number seen in Fig. 1) of the observations.

circumplanetary flow or volcanic plumes will become less porous as the relatively high temperatures during the day allow molecules to break their bonds with the surface, migrate down through the pores of the frost, and eventually fill the pores. The best fit thermal inertia we obtain, $\Gamma_F \sim 200 \text{ J m}^{-2} \text{ K}^{-1} \text{ s}^{-1/2}$, also agrees with recent observations and subsequent fits of Io's atmospheric column density variation with heliocentric distance (Tsang et al., 2012). The resulting SO_2 surface frost temperature distribution as a function of latitude and longitude with the best fit frost thermophysical parameters and for a subsolar longitude of 180°W is shown in Fig. 5.

With the best fit thermophysical parameters, the peak T_F is $\sim 119.4 \text{ K}$ on the anti-jovian hemisphere which is slightly higher than the values of 116.7 K (for a latitudinal fit) and 118 K (for a solar zenith angle fit) derived by Jessup et al. (2004) based on VPE. This discrepancy is because the best fit overestimates the peak T_F in order to fit the data points at mid to high solar zenith angles. The effects of vapor pressure non-equilibrium are quite small (in the region around the peak T_F) as shown in Fig. 2. The departure of the column density from VPE is less than 10% at the location of the peak T_F and everywhere between 180°W and 90°W at low to mid-latitudes. The relatively high Γ_F causes a phase lag between the subsolar point (180°W) and the peak T_F equal to $\sim 33^\circ$ which is

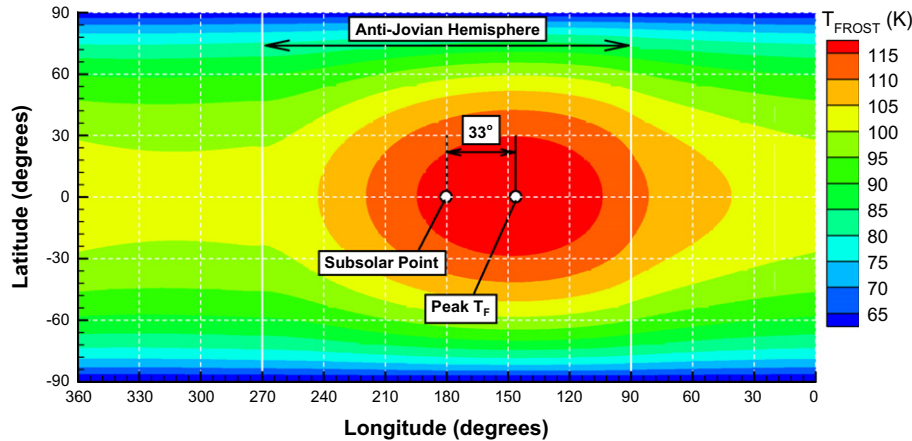


Fig. 5. The SO_2 surface frost temperature as a function of latitude and longitude. The subsolar point and peak T_F are labeled by white circles. The relatively high thermal inertia of the frost leads to a large thermal lag of 33° between the subsolar point and the peak temperature.

close to the value of 32° found by Walker et al. (2010). The subsolar temperature is ~ 117.3 K (2.1 K colder than the peak T_F).

Fig. 6 shows three longitudinal T_F profiles at 30° intervals of latitude starting at the equator (0°N , 30°N , 60°N) at a subsolar longitude of 180°W . The equatorial T_F reaches a minimum of 101.1 K approximately 30° (~ 3 h) before dawn. Just before dawn, $T_F = 101.6$ K. This does not mean that the given location on the surface is actually warming as it approaches dawn but that the points nearer the anti-jovian hemisphere are warmer than those further away. This is another effect of eclipse which will be discussed in Section 3.1.2. The peak T_F of the profile at 30°N is 4.9 K cooler (114.5 K) than the equatorial profile. At all longitudes on the nightside, the 30°N profile is ~ 3.0 K cooler than the equatorial profile. Lastly, the 60°N profile shows much lower temperatures and smaller diurnal variation as expected due to the smaller amount of absorbed sunlight. The peak T_F drops to 98 K and has a minimum of 88 K during the night.

Next, we examine the latitudinal dependence of the frost temperature distribution at 180°W subsolar longitude. Fig. 7 shows three latitudinal T_F profiles for selected longitudes (peak T_F , subsolar longitude, and sub-jovian point). The equatorial temperatures have already been discussed so we focus on mid- to high latitudes. Near the poles, T_F drops to ~ 60 K due to the very low diurnally-averaged solar flux for all longitudes. 60 K is colder than observed

by the Galileo spacecraft's PPR (Rathbun et al., 2004) and it may be that the poles are areas of excess (un-modeled) endogenic heating as discussed by Rathbun et al. (2004) or there may be excess (un-modeled) plasma heating near the poles. From the polar region, mid-latitudes quickly warm to brightness temperatures observed by the Galileo PPR (Rathbun et al., 2004). At $\pm 70^\circ\text{N/S}$, the observed dayside T_B is ~ 100 K at the subsolar longitude while the nightside T_B is ~ 85 K (see Fig. 6 in Rathbun et al. (2004)). In comparison, simulated dayside T_B is ~ 95 K at the subsolar longitude and nightside T_B of ~ 75 – 85 K (depending on the local time of day). The sub-jovian point's equatorial T_F is ~ 102 K which is 17 K colder than the peak T_F on the dayside (see Figs. 6 and 7).

3.1.2. Non-frost best fit parameters

The best fit for the non-frost thermophysical parameters is shown in Fig. 8a. The best fit occurs at $\alpha_{NF} \approx 0.49$ and $\Gamma_{NF} \approx 20 \text{ J m}^{-2} \text{ K}^{-1} \text{ s}^{-1/2}$. As discussed earlier, the best fit α_{NF} is fixed once the best fit α_F is chosen and therefore only Γ_{NF} remains as a free parameter. A larger range of Γ_{NF} was studied than shown in Fig. 8a and the error was seen to monotonically increase away from the best fit Γ_{NF} (e.g. no other minima were found). A comparison to the brightness temperature, T_B , computed from observations made by the Galileo PPR (Rathbun et al., 2004) is shown in Fig. 8b.

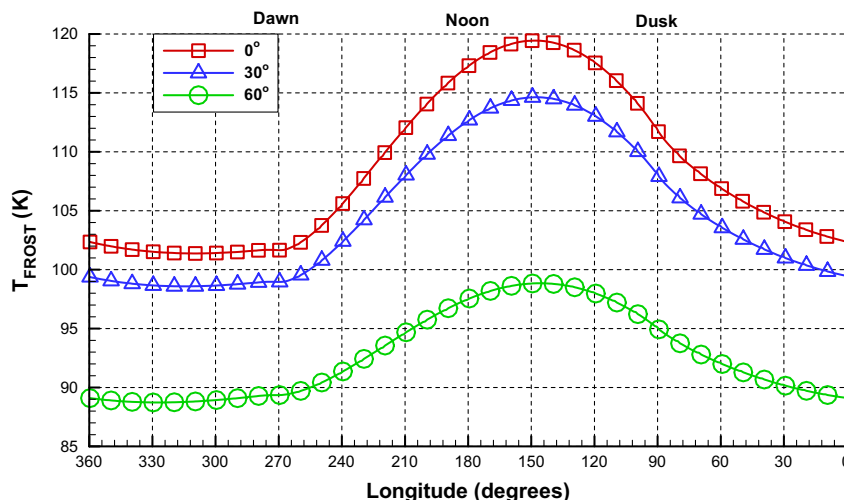


Fig. 6. SO_2 frost surface temperature profiles as a function of longitude for selected latitudes of 0° , 30° , and 60° .

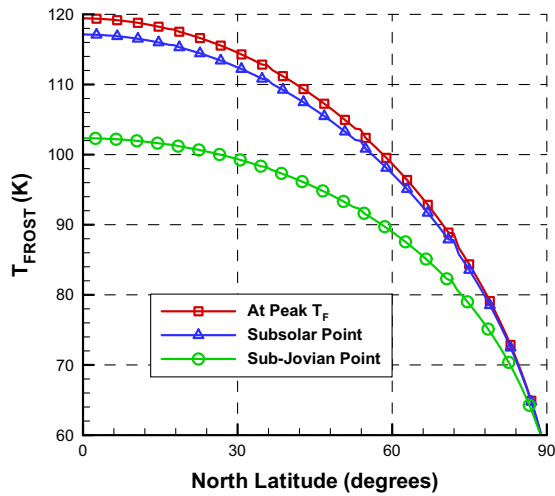


Fig. 7. SO₂ frost temperature profiles as a function of latitude extracted at the longitudes of several points on Io's surface: the peak T_F , the subsolar longitude (also the anti-jovian point), and the sub-jovian point (at midnight).

The peak T_B for the observation is ~ 130 K and the simulation overestimates the data by ~ 2 K. The main regions of discrepancy occur during the night (at “times of day” between 15° and 195° W). The simulated brightness temperature is slightly too high

just after dusk and before midnight but too low after midnight and before dawn. Better fits to the nightside cooling rate were achieved using a lower (but unphysical) frost albedo with a higher thermal inertia. The minimum T_B (~ 96 K) for the observation occurs just before dawn but is ~ 3 – 4 K lower in the simulation. The spike in the observation at $\sim 210^\circ$ W is a hot spot.

The very low thermal inertia of the non-frost surface indicates that it must be composed of fine-grained particulates. These are likely to be pyroclastic dusts (Rathbun et al., 2004) ejected from the many volcanic plumes on Io or sulfur allotropes (also originating from volcanic plumes) which are a major constituent of the reflectance spectra. This apparent high porosity is self-consistent with the need for a “long residence time” model found by Walker et al. (2010) to explain the observed sub-jovian/anti-jovian asymmetry in the mid-infrared (Spencer et al., 2005). In the long residence time model, molecules are assumed to become trapped in a porous solid for many absorptions/desorptions until they eventually escape the lattice. The very low Γ_{NF} will result in the non-frost surface remaining close to radiative equilibrium (the limiting case for $\Gamma_{NF} = 0$).

Next, we examine T_{NF} rather than T_B (T_B includes the effect of both the frost and non-frost surfaces). Currently, T_{NF} , which is used to determine the thermal inertia of the non-frost, can only be inferred from knowledge of our simulated T_F and the observed T_B . With much higher spatial resolution in future observations, it may be possible to isolate frost deficient regions in which the brightness temperature would essentially be the non-frost

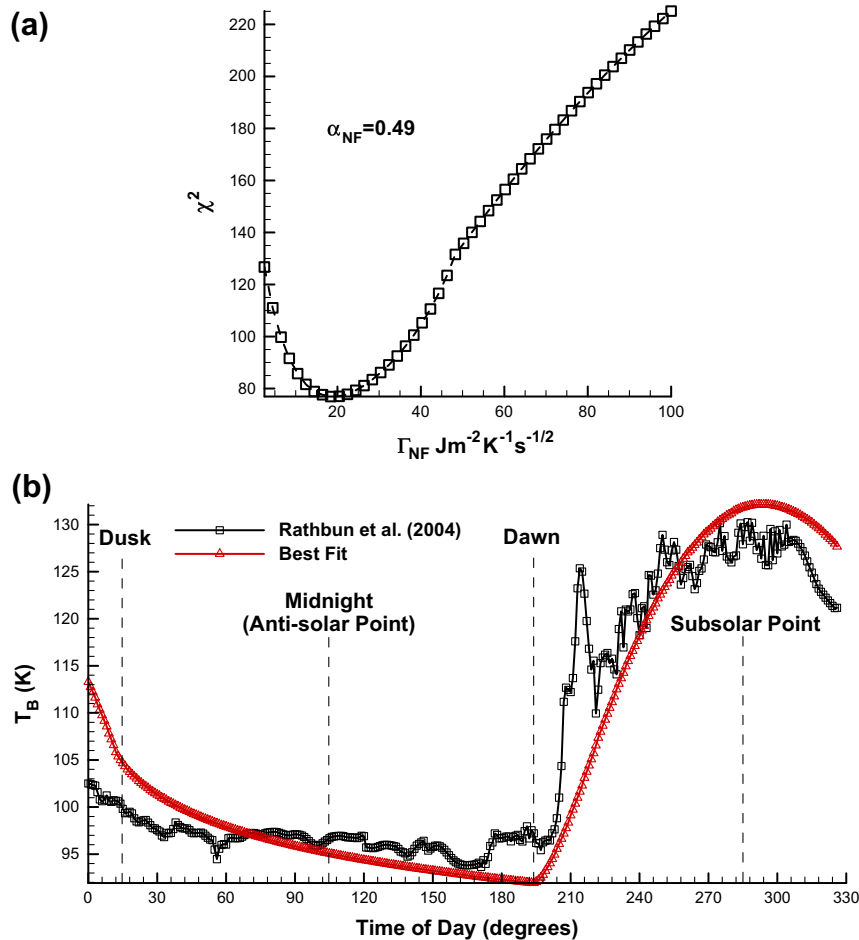


Fig. 8. (a) χ^2 as a function of non-frost thermal inertia, Γ_{NF} . The non-frost albedo, α_{NF} is constrained to be 0.49 by the frost albedo and mean frost fraction. The best fit occurs at $\Gamma_{NF} \sim 20 \text{ J m}^{-2} \text{ K}^{-1} \text{ s}^{-1/2}$. (b) A comparison between observed (Rathbun et al., 2004) and simulated brightness temperatures. The best fit appears to slightly overestimate temperatures just after dusk (~ 30 – 60° W) and underestimate temperatures just before dawn (~ 120 – 180°). The spike at $\sim 210^\circ$ is Prometheus.

temperature, T_{NF} . In the simulated temperature distribution, the peak T_{NF} is 143.2 K and lags the subsolar point (which is located at the anti-jovian point for this case) by $\sim 11^\circ$ (see Fig. 9). This phase lag due to the Γ_{NF} is small but not insignificant and corresponds to the peak T_{NF} occurring ~ 1 h and 15 min after high noon. In comparison, the peak T_F occurs 33° or ~ 3 h and 50 min after high noon. Due to the relatively small Γ_{NF} the temperature difference between the subsolar point ($T_{NF} = 142.6$ K) and the peak T_{NF} is only 0.6 K.

T_{NF} is shown as a function of longitude for three selected latitudes (0°N , 30°N , and 60°N) in Fig. 10. Comparing the peak T_{NF} for the mid- and high latitude slices with the equatorial slice, T_{NF} peaks at 137.6 K at 30°N and at 117.7 K at 60°N . The much higher peak T_{NF} compared to T_F at mid-latitudes is due in small part to the lower albedo but is largely due to the very low Γ_{NF} that creates a larger diurnal temperature variation. The nightside temperatures only differ by 1.1–1.7 K between the equator and 30°N depending on the local time of day. At 60°N , the temperatures are significantly lower and have a smaller variation as a function of time of day; during the night, T_{NF} is 5.2–8.5 K colder than the equatorial temperatures. Unlike T_F which reaches a minimum a significant time (~ 3 h) before dawn, T_{NF} decreases monotonically during the night and reaches its minimum temperature (regardless of latitude) just before dawn. This is because the lower Γ_{NF} leads to a much larger temperature variation during the night and therefore the variation in total insolation absorbed is less extreme. The T_{NF} minima just before dawn are 75.4 K, 74.3 K, and 70.2 K for 0°N , 30°N , and 60°N , respectively.

Lastly, the latitudinal temperature variation of T_{NF} is described. Latitudinal profiles at selected longitudes (peak T_{NF} , subsolar longitude/anti-jovian point, and sub-jovian point) are shown in Fig. 11. The small thermal lag arising from Γ_{NF} results in the latitudinal profiles at the peak T_{NF} and at the subsolar point that are nearly identical at all latitudes. The sub-jovian point latitudinal profile has large differences from the two dayside profiles. To reiterate, the sub-jovian point is midnight for the current simulated temperature distribution and therefore T_{NF} on the equator is very low (81.4 K). At higher latitudes, T_{NF} falls off more slowly than the dayside profiles because the endogenic heating term is constant with latitude, the radiation flux from Jupiter (~ 0.67 W m $^{-2}$) is less than the endogenic heating, and the insolation heating term is zero at this instant. The temperature variation is due to the residual thermal energy collected during the day that has not been emitted. If the sub-jovian point were hypothetically to stay in constant

darkness, the latitudinal profile would eventually become nearly uniform. The minimum (polar) temperature would depend only on the endogenic heating rate (1.0 W m $^{-2}$) and the radiation flux from Jupiter (~ 0.67 W m $^{-2}$) would give a very slight temperature (~ 1 K) increase near the equator. The polar T_{NF} is ~ 55 K for all cases.

It should be noted that Io has 100–150 mountains which average 6 km in altitude and reach up to 17 km in altitude (Schenk et al., 2001); however, in the current model Io is assumed spherical. When these topographical features lie near the terminator, they can shadow a substantial area of the dayside up to $\sim 5^\circ$ (150 km) away from the terminator. For the non-frost surface, which responds quickly to changes in insolation, these shadows could create local variations in T_{NF} .

3.1.3. Effects of eclipse

Lastly, we investigate the temperature variation during and due to eclipse. An important asymmetry in the anti-jovian (centered at 180°W) and sub-jovian (centered at 0°W) temperature distributions is created due to eclipse. Since Io is tidally locked, only the sub-jovian side experiences eclipse and therefore has a decreased net solar flux averaged over its day compared to the anti-jovian hemisphere. This difference in diurnally integrated solar flux leads to lower temperatures on the sub-jovian hemisphere even outside of eclipse; therefore, the sub-jovian hemisphere will have a thinner atmosphere with a lesser latitudinal extent than the anti-jovian hemisphere. This asymmetry has been observed in the mid-infrared (Spencer et al., 2005), Lyman- α (Feaga et al., 2009), and millimeter range (Moulet et al., 2008). Previously, the sub-jovian/anti-jovian asymmetry has been explained by the biased distribution of volcanic plumes (with more active volcanic plumes existing on the anti-jovian hemisphere than on the sub-jovian hemisphere) or by the inhomogeneous SO_2 frost distribution (Douté et al., 2001). The volcanic plumes and inhomogeneous surface frosts likely play a role in the asymmetry, but we suggest that an additional explanation for the sub-jovian/anti-jovian column density asymmetry is the fact that the sub-jovian hemisphere experiences eclipse (Tsang et al., 2012).

In Fig. 12a, equatorial T_F profiles before and at several times during eclipse are shown. Immediately prior to entering eclipse, the peak T_F is 118.5 K. This temperature is 0.9 K cooler than the corresponding peak T_F on the anti-jovian hemisphere. The temperature difference between the peak T_F on the anti-jovian and sub-jovian hemispheres is due to eclipse even though the peak on the

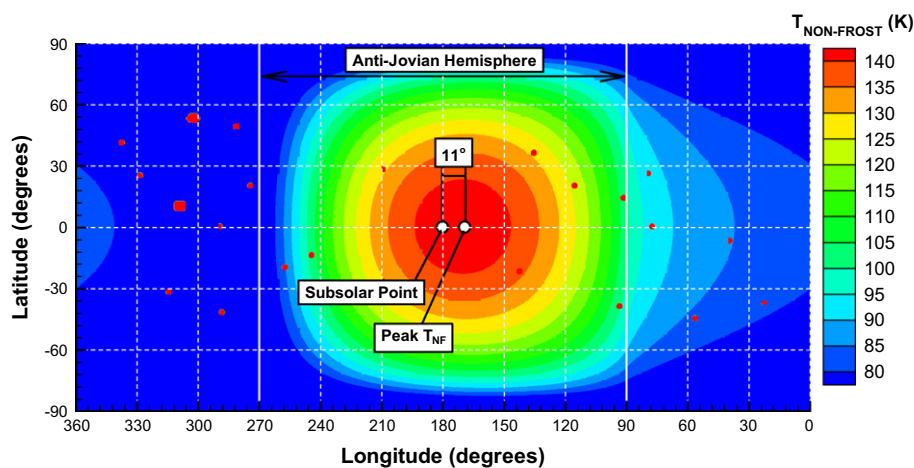


Fig. 9. The non-frost surface temperature as a function of latitude and longitude. The subsolar point and peak T_{NF} are labeled by white circles. There is only a small thermal lag of 11° between the subsolar point and the peak T_{NF} . Each red (saturated) spot corresponds to a hot spot on Io's surface. See Section 2.6 for the definition of hot spots in our model. (For interpretation of the references to color in this figure legend, the reader is referred to the web version of this article.)

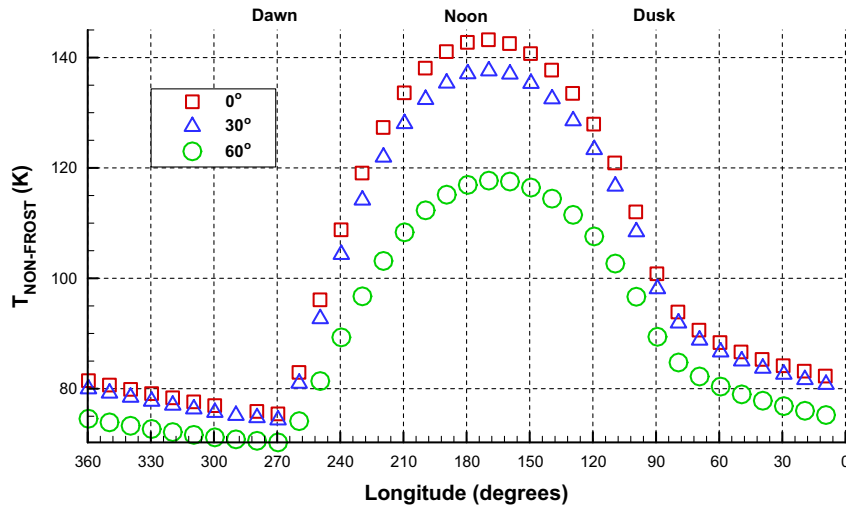


Fig. 10. Non-frost surface temperature profiles as a function of longitude for selected latitudes of 0°, 30°, and 60°.

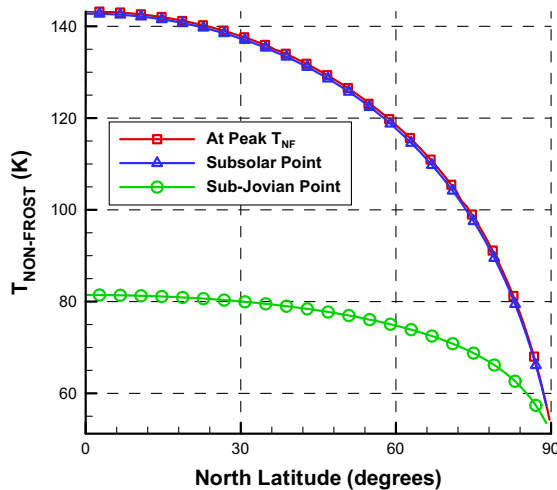


Fig. 11. Non-frost surface temperature profiles as a function of latitude extracted from Fig. 9 at the longitudes of several points on Io's surface: the peak T_{NF} , the subsolar longitude (also the anti-jovian point), and the sub-jovian point (at midnight).

sub-jovian hemisphere is pre-eclipse. As previously stated, the sub-jovian hemisphere will experience less net sunlight through its day due to eclipse. The effect of eclipse will also be strongest at the sub-jovian point and diminish with solar zenith angle away from it. At the sub-jovian point, the amount of sunlight lost during the 2 h eclipse is $\sim 15\%$ of the total insolation. The diurnal temperature variation is dependent on the total insolation absorbed by the surface and this will be lower on the sub-jovian hemisphere than on the anti-jovian hemisphere which sees the sunlight throughout its daylight hours. The blackbody radiation emitted from Jupiter's atmosphere heats the sub-jovian hemisphere's surface and partially compensates for the cooling due to eclipse; however, eclipse is the dominant effect. The diurnally averaged radiation emitted by Jupiter's atmosphere and then absorbed by Io's surface ($\sim 0.67 \text{ W m}^{-2}$ over the entire rotation or $\sim 28.1 \text{ W h m}^{-2}$) is equivalent to $\sim 25\%$ of the sunlight lost due to eclipse ($50\text{--}55 \text{ W m}^{-2}$ for 2 h or $100\text{--}110 \text{ W h m}^{-2}$) at the sub-jovian point.

During eclipse, the peak T_F cools from 118.5 K to 115.1 K, 113.0 K, 111.8 K, 110.8 K after 10, 43, 77, and 110 min in eclipse, respectively. Based on VPE, these temperatures correspond to column densities of

$2.3 \times 10^{17} \text{ cm}^{-2}$, $7.6 \times 10^{16} \text{ cm}^{-2}$, $3.7 \times 10^{16} \text{ cm}^{-2}$, $2.4 \times 10^{16} \text{ cm}^{-2}$, $1.7 \times 10^{16} \text{ cm}^{-2}$, respectively; however, during eclipse VPE will not hold because it assumes that the information (temperature change of the surface) can propagate instantaneously to the gas. Due to the finite speed of sound in the gas (130–350 m/s, depending on the local gas temperature), there will be a lag between the cooling T_F and its effect upon the overlying SO_2 gas column density of the atmosphere. This effect was investigated in the presence of a non-condensable species by Moore et al. (2009). The VPE column densities computed above will be compared in Section 3.2.1 to the actual column densities calculated from the DSMC atmospheric simulations.

Another interesting phenomenon that occurs during eclipse is that the location of the peak T_F moves in the prograde direction (see Fig. 12). This is opposite to the direction that the peak T_F moves outside of eclipse (retrograde direction). The two causes of this phenomenon both depend on the state of the thermal wave. The thermal wave, seen in Fig. 13a, is the temperature of the solid material (frost or non-frost) as a function of depth into the solid. The first cause is that the thermal wave has not yet reached a steady state (e.g. has not penetrated as deeply into the solid) in regions closer to dawn (see Fig. 13a). In these regions, the time in sunlight is less than the heat conduction timescale. This effect can also clearly be seen in Fig. 13b which shows a phase lag between solid frost temperatures at depth and the surface frost temperature for a subsolar longitude of 325°W . The second cause is that eclipse most strongly affects areas near the sub-jovian point. The deficit of net absorbed sunlight leads to a slightly lower “deep temperature” for regions nearer the sub-jovian point compared to those on the anti-jovian hemisphere. When eclipse occurs and heating from insolation disappears, each surface area element will radiate at a rate dependent on the state of the thermal wave within the surface. In the absence of the insolation, the regions with the largest energy content (integrated with depth) will tend to have the highest surface temperatures after a time longer than the heat conduction timescale. Fig. 13a shows the temperature profile with depth into the surface at both 120° and 140°W at two different times (10 min prior to eclipse and 93 min into eclipse). The figure shows that the point at 120°W has a lower surface temperature before eclipse but near the end of eclipse (at 93 min) it has a warmer surface temperature than that of the surface at 140°W . The same effect can be seen in Fig. 13b near the dusk terminator at 60°W .

Changes in T_{NF} are shown in Fig. 12b at the same selected times as the T_F data of Fig. 12a. The non-frost surface experiences larger temperature variations because of the lower Γ_{NF} . After 10 min in

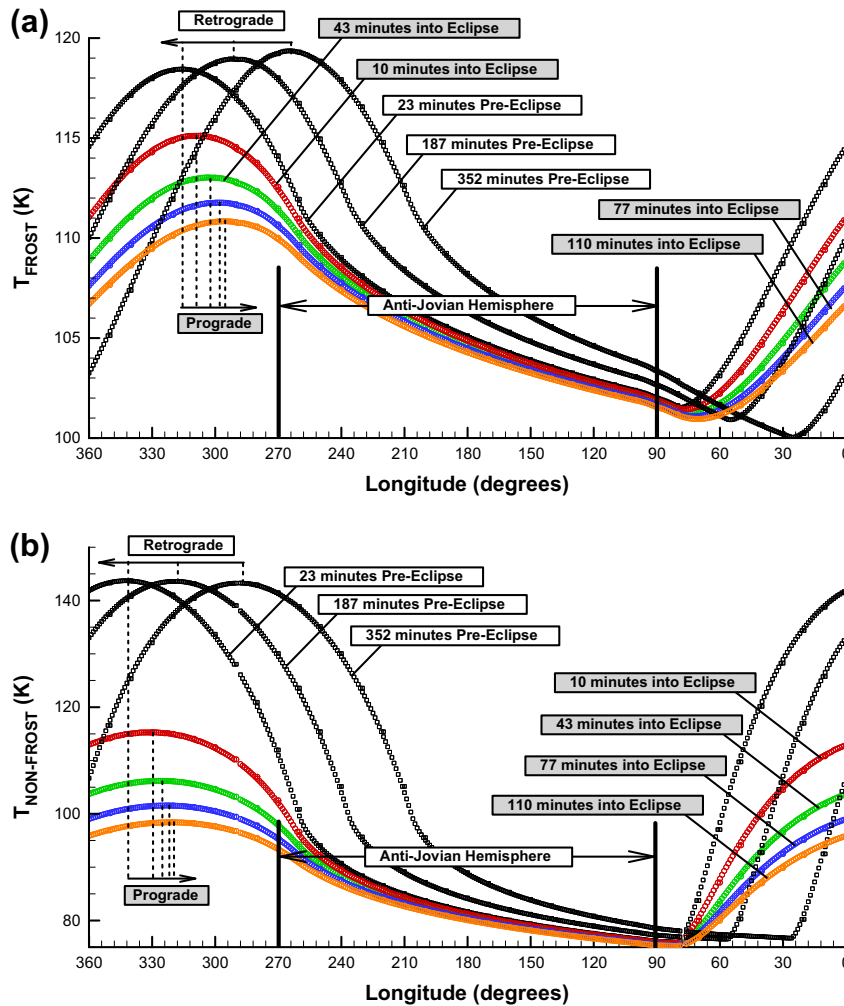


Fig. 12. Equatorial temperature profiles for (a) T_F and (b) T_{NF} at several times before and during eclipse. The selected times shown are 23, 187 and 352 min prior to eclipse. Selected post-eclipse times shown are 10 min, 43 min, 77 min, and 110 min into eclipse.

eclipse, the peak T_{NF} decreases to 115.2 K. The successive peak T_{NF} throughout eclipse are 106.2 K, 101.8 K, 98.5 K at 43, 77, and 110 min into eclipse, respectively. The peak T_{NF} also has a similar prograde rotation as T_F during eclipse.

When the sub-jovian hemisphere exits eclipse it takes several hours for the frost surface to recover to its quasi-steady equilibrium state that existed before eclipse. This can be quantified by the “thermal parameter” defined by (Spencer et al., 1989):

$$\theta = \frac{\Gamma\sqrt{\omega}}{\varepsilon\sigma T^3} \quad (12)$$

The thermal parameter takes the ratio of the characteristic time scale for the surface to radiate a particular amount of heat to the diurnal timescale. When $\theta = 0$, the surface is in instantaneous radiative equilibrium with the insolation, whereas $\theta = \infty$ corresponds to a surface where temperature is only a function of latitude and independent of time of day. To estimate the thermal parameters for both the SO_2 frost and non-frost surfaces, we choose temperatures near high noon. Assuming $T_F \sim 115$ K and $T_{NF} \sim 140$ K, then is $\theta_F \sim 14.9$ and $\theta_{NF} \sim 0.82$, respectively.

Before ingress into eclipse, T_F is ~ 118.5 K (Fig. 12a) but 2 h after lo exits eclipse the peak T_F has only warmed to ~ 114.5 K (Fig. 14a). T_{NF} responds much more quickly due to its low Γ_{NF} and recovers within ~ 1.5 K of the pre-eclipse peak value 2 h after egress from eclipse (see Fig. 14b). The peak T_{NF} increases rapidly when the non-frost is exposed to sunlight and only 23 min after egress from

eclipse, the peak T_{NF} has risen ~ 34 K. Further inhomogeneous thermal structure due to eclipse can be seen in Fig. 14a between 270°W and 300°W . Unlike the pre-eclipse equatorial thermal profile that decreases monotonically with decreasing longitude on the night-side, the post-eclipse thermal profiles show an unusual structure due to the variation in the “deep temperature” between 270°W and 300°W . As described earlier, points further from the sub-jovian hemisphere will absorb more sunlight throughout the day and therefore will have a higher “deep temperature”. The variation in “deep temperature” also causes some unusual structure in the thermal profiles between 60°W and 90°W .

The asymmetry between the anti-jovian and sub-jovian points can be seen most clearly by comparing their temperature profiles as a function of time of day. In Fig. 15a, the difference in the peak T_F between the sub-jovian and anti-jovian point is ~ 4.2 K. The anti-jovian point peaks at ~ 119.5 K at ~ 30 h while the sub-jovian point peaks at ~ 115.1 K at ~ 10 h. If these T_F are converted to column densities assuming VPE, this corresponds to column densities of $7.63 \times 10^{16} \text{ cm}^{-2}$ at the sub-jovian point and $3.23 \times 10^{17} \text{ cm}^{-2}$ at the anti-jovian point. Based on these estimated VPE column densities, the anti-jovian point will have a peak column density $\sim 4.2 \times$ larger than sub-jovian point. Note that on this time axis, eclipse occurs between approximately 4 and 6 h.

The effect of eclipse can also be seen on the nightside where T_F is ~ 2 K lower for the sub-jovian point compared to the anti-jovian point. This 2 K difference is nearly constant for all times of day and

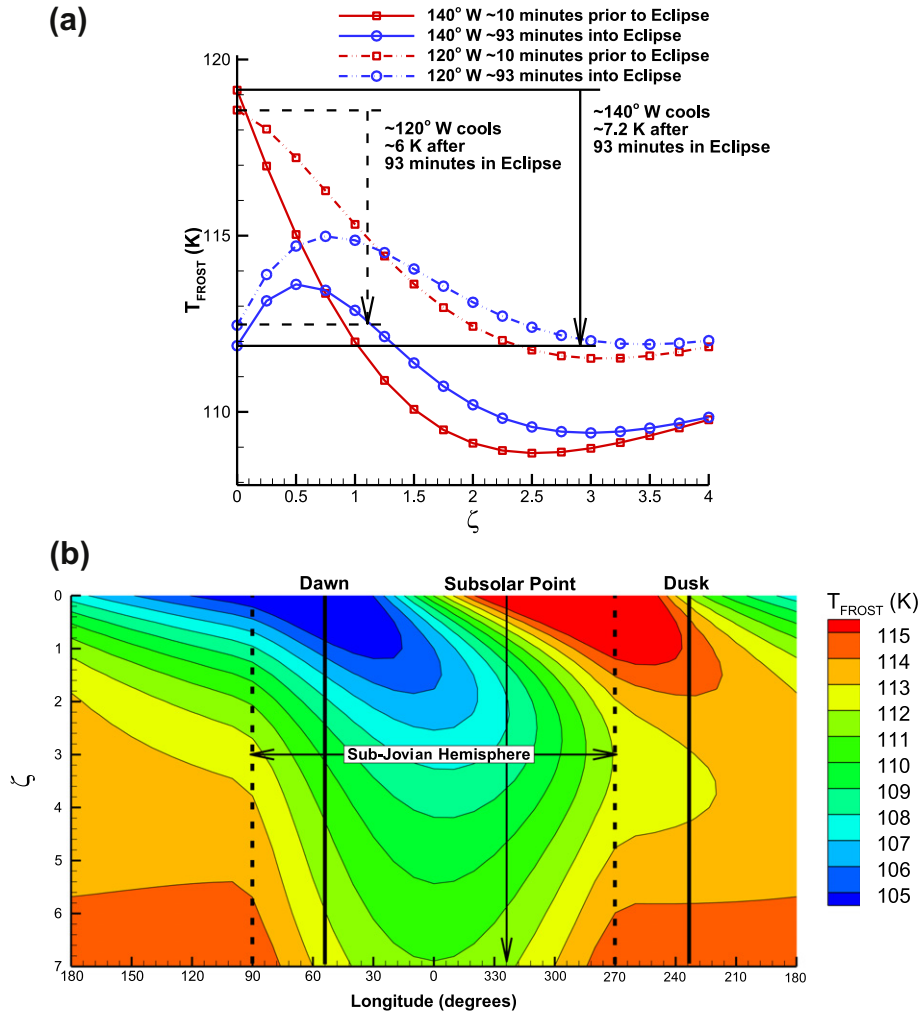


Fig. 13. (a) A comparison between the temperature as a function of depth at two different longitudes along the equator before and in eclipse. 140°W (solid lines) has a higher surface temperature initially but lower temperature at depth whereas the point 120°W (dashed lines) has a lower surface temperature but higher temperatures at depth. Throughout eclipse the point with the higher “deep temperature” at 120°W of the subsolar point cools more slowly and ends up with a higher surface temperature near the end of eclipse. The ζ range has been truncated to highlight the near surface features. (b) The temperature of the SO₂ frost solid as a function of depth and longitude at the equator for a subsolar longitude of 325°W.

can also be seen in Fig. 15b where the phase difference between the anti-jovian and sub-jovian points has been removed such their “noon” occurs at the same time of day on the x -axis. Eclipse does not occur centered on Fig. 15b because of the thermal phase lag from the high Γ_F which means that the frost temperatures are shifted more than 180° to remove the phase difference between the sub-jovian and anti-jovian points assumed peaks.

3.2. DSMC computed atmosphere

Global DSMC atmospheric simulations were carried using the solid surface boundary conditions for the frost and non-frost described in Section 3.1. The simulation results presented describe the dayside atmospheric structure for over 6 h around eclipse (~2.5 h before, ~2 h in eclipse, and ~2 h after eclipse) and at a single instant for the anti-jovian hemisphere. The resulting column densities, number densities, temperatures (translational, rotational, and vibrational), and global winds (velocities, Mach numbers, and streamlines) will be described. To begin the discussion, the simplest quantity, vertical SO₂ gas column density, will be described since it is inherently two-dimensional.

3.2.1. Atmospheric SO₂ gas column density

Before eclipse, dayside column densities are largely in VPE with the SO₂ surface frosts as illustrated by the elliptical shape of the column density contours that follow the same shape as T_F contours (see Fig. 16). The only region of substantial departure from VPE is near the dawn terminator where a significant portion of the atmosphere is sustained by desorption from the non-frost surface. As detailed in Walker et al. (2010), the interaction between SO₂ gas and the non-frost surface leads to SO₂ molecules condensing on the non-frost surface during the night when it is cool. The condensed gas then rapidly desorbs near dawn when the non-frost surface warms quickly, creating an enhanced atmosphere near dawn (DAE).

The majority of the atmosphere is in a quasi-steady state during the two and a half hours simulated prior to eclipse. The morphology of the dayside atmosphere remains essentially constant as the subsolar point rotates toward eclipse. The only region where significant unsteadiness exists prior to eclipse is near the DAE. These variations are caused by inhomogeneous surface frosts and the complicated dynamics of non-frost thermal distribution in eclipse and leaving eclipse. As noted in Section 3.1, the peak T_{NF} has a prograde rotation during eclipse and when Io exits from eclipse the

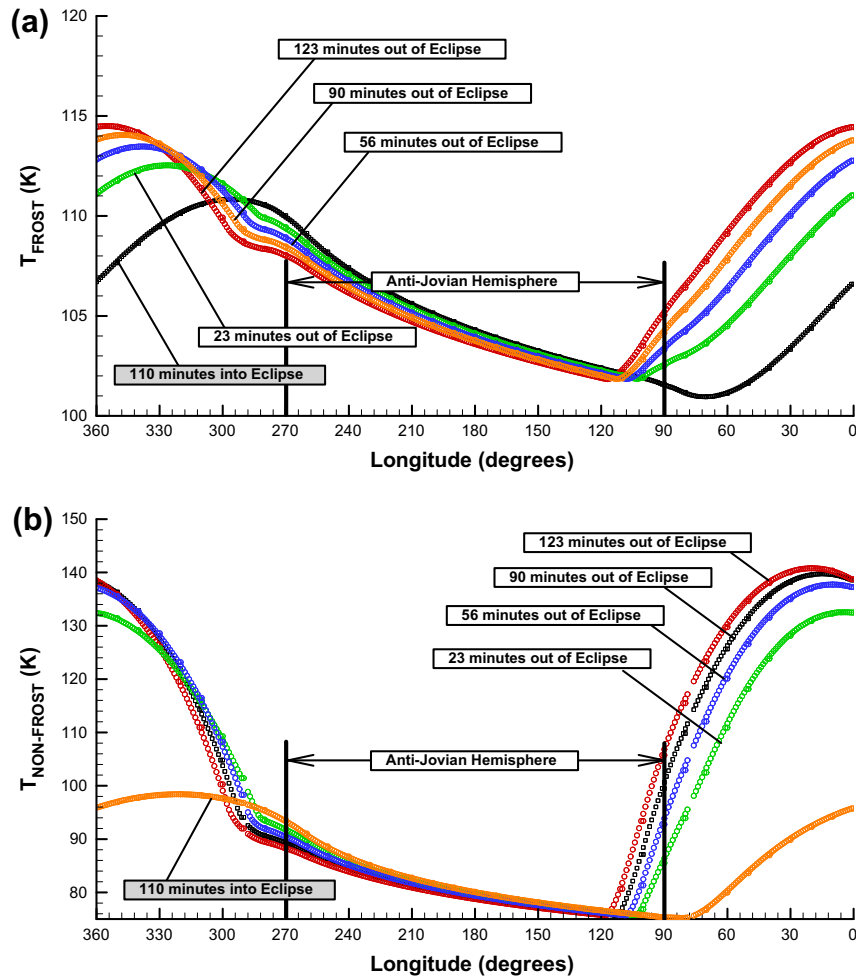


Fig. 14. Equatorial temperature profiles for (a) T_F and (b) T_{NF} at several times during and after eclipse. The selected times shown are 110 min into eclipse (~ 10 min before egress), 23 min, 56 min, 90 min, and 123 min after egress from eclipse.

peak rapidly sweeps back in a retrograde rotation to its quasi-steady location. In the process, the non-frost surface is thoroughly denuded of SO_2 molecules since the timescale for desorption is very short compared to the timescale on which the peak T_{NF} returns to its quasi-steady state location. At the same time, the peak T_F for the SO_2 frost surface also sweeps quickly back to its quasi-steady state location but this timescale is short compared to the time required to re-cover the non-frost surface with a thin film of SO_2 molecules. Therefore, the non-frost region of the sub-jovian hemisphere between 300° and 360°W has a lower density of SO_2 molecules absorbed on the surface.

The DAE is quite small 2.5 h prior to eclipse because this area of the non-frost surface is thoroughly denuded of SO_2 molecules. As the atmosphere approaches ingress, the DAE grows in size because the density of SO_2 molecules adsorbed on the non-frost also grows. This situation of a quasi-steady bulk atmosphere and slightly unsteady DAE (which grows as eclipse approaches) continues up until ingress into eclipse. The peak column density, N_C , is $\sim 2.6 \times 10^{17} \text{ cm}^{-2}$ 2.5 h prior to eclipse, and decreases slightly as the atmosphere approaches ingress. Just prior to ingress, the peak N_C has dropped to $\sim 2.2 \times 10^{17} \text{ cm}^{-2}$ due to the lower SO_2 frost fraction and slightly cooler T_F due to diurnally averaged effect of eclipse lowering the amount of sunlight absorbed on the sub-jovian hemisphere.

When Io enters eclipse, the atmosphere begins to collapse but is constrained by the atmospheric speed of sound. The SO_2 gas that

condenses on the non-frost will stick for a residence time dependent on the cooling T_{NF} . Just prior to eclipse, the non-frost surface region around the peak T_{NF} ($\sim 143 \text{ K}$) remains denuded of SO_2 because the residence time at that temperature is $\sim 1.3 \text{ s}$. 10 min into eclipse, the peak T_{NF} has cooled to $\sim 115 \text{ K}$ which corresponds to a residence time of $\sim 7.7 \text{ h}$. As the surface continues to cool, the residence time grows exponentially (Eq. (11)). The lengthened residence time (longer than an Io day near end of eclipse) means that nearly all of the SO_2 gas which lands on the non-frost surface will condense and stick for the remainder of eclipse.

During eclipse, the column density decreases due to the cooling T_F and T_{NF} . Comparing the DSMC calculated column density (which includes speed of sound effects) with VPE column density based on T_F , we expect that the DSMC column density will be higher due to the finite response time. However, Fig. 17 plots the column density as a function of time during eclipse at the location of the peak N_C just prior to eclipse and shows that the DSMC calculated column density actually falls quicker than expected from VPE with the SO_2 frost. The reason for this is a significant portion of the atmosphere is sustained by molecules “hopping” off the warm ($\sim 140 \text{ K}$) non-frost surface and VPE assumes that the entire column is sustained by instantaneous response to the frost surface alone. During eclipse, the non-frost surface cools much quicker due to its very low Γ_{NF} and therefore its contribution to the local atmosphere will disappear quickly. In this case, the timescale for the changes in T_{NF} are much shorter than T_F and therefore the

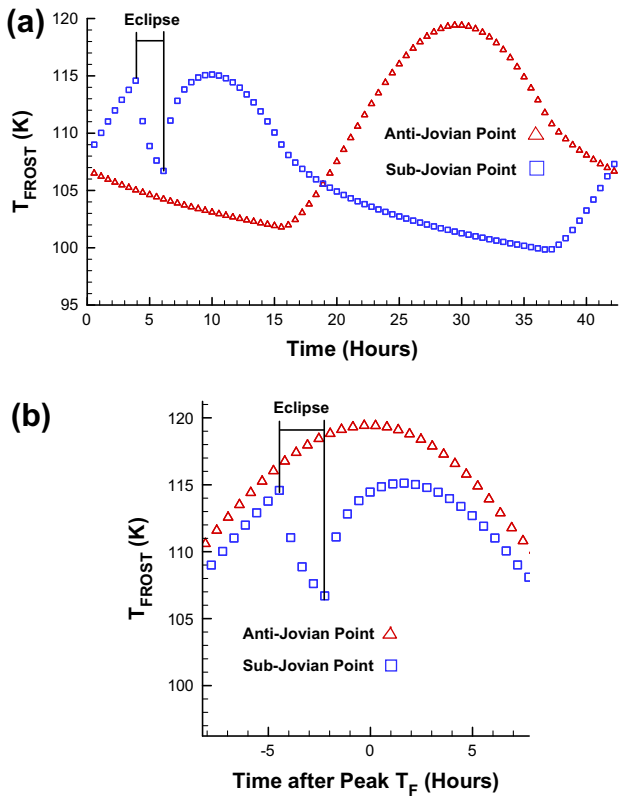


Fig. 15. (a) A comparison between T_F at the anti-jovian and sub-jovian points as a function of time of day. Both the sub-jovian and anti-jovian hemispheres are simulated at their respective high noon. (b) The same data but now with the phase shifted such that the peaks (if eclipse did not occur) coincide and the x-axis reduced to highlight eclipse. The sub-jovian point is most strongly affected by eclipse.

column density decreases more rapidly than expected for VPE based on T_F .

Near the beginning of eclipse, the VPE and DSMC computed column densities overlap because both are limited by the speed of sound. After ~ 15 min, the DSMC column density diverges from VPE. This occurs because VPE is constrained by the high Γ_F rather than the speed of sound whereas the low Γ_{NF} causes T_{NF} to decrease rapidly and therefore the collapse of the atmosphere is limited only by the speed of sound. After eclipse, the DSMC computed column density overshoots VPE because the excess SO_2 gas that condensed on the non-frost surface quickly desorbs as the surface warms. Moore et al. (2009) simulated the one-dimensional collapse of Io's atmosphere including the effects of non-condensable species. They found that a small concentration of non-condensable can considerably slow the collapse of the atmosphere by creating a diffusion layer near the surface.

The influence of Loki can be seen in nearly all the snapshots of Fig. 16 at $(10^\circ\text{N}, 310^\circ\text{W})$. Prior to eclipse, the column density above Loki is lower than over the surrounding areas because it is so warm (>300 K) that any SO_2 frosts are rapidly sublimated away. Therefore, no sublimation occurs from Loki's disk because it has no SO_2 frost. During eclipse, both the frost and non-frost surfaces cool whereas Loki remains at a constant temperature since its temperature is sustained by volcanism rather than insolation. Since Loki remains at a constant temperature and covers such a large area, molecules that are temporarily "trapped" hopping around on the hot surface will not condense and therefore an inflection occurs where the column density above Loki decreases much more slowly than over the surrounding areas. Loki's column density will only decrease as molecules diffuse off of its hot disk onto the

surrounding cold surfaces. This diffusion occurs approximately at a linear rate and therefore at the beginning of eclipse, Loki will have a higher column density but as the frost and non-frost surface cool slowly, Loki's column density will continue to decrease and eventually drop below that of the surrounding areas. As discussed in Walker et al. (2011), the pressure over Loki does not quickly equilibrate with the local sublimation atmosphere because the ballistic length scale, $d_B = 8H/\pi$, is smaller than the mean radius of the hot spot. This is in agreement with the earlier work of Ingersoll (1989) who defined a horizontal averaging length scale, $L = \sqrt{2\pi}H \approx d_B$, over which local frost patches control the pressure. Other hot spots are more difficult to see in Fig. 16 because many are small compared to the lateral cell size (30 km at the equator). Just after ingress into eclipse, for example, Fuchi is visible at $(25^\circ\text{N}, 328^\circ\text{W})$ in Fig. 16i and j when the surrounding column densities are collapsing more rapidly than the atmosphere over the hot spot due to its constant temperature.

After egress from eclipse, it requires approximately 2 h for the atmosphere to return to its pre-eclipse morphology. During those 2 h, the atmosphere has a very complex structure that is due to the underlying changes in surface temperature (both frost and non-frost). Because of the lower Γ_{NF} , T_{NF} increases more rapidly than T_F . During eclipse, a significant amount of the column ($\sim 90\text{--}95\%$) condenses onto the surface and approximately half of that will land on the non-frost surface. After egress from eclipse, this material will rapidly desorb from the non-frost surface over much of the dayside but the desorption will be centered over the peak T_{NF} which occurs $\sim 10^\circ$ east of the subsolar point. Because the amount of material condensed on the non-frost surface is finite ($\sim 10^{16}$ cm^{-2}), nearly all of the SO_2 will desorb from the non-frost surface within ~ 30 min after egress. The frost surface responds more slowly due to its high Γ_F and therefore its contribution to the atmosphere is masked by desorption from non-frost surface until ~ 30 min after eclipse. Due to these different response rates, the atmosphere has a very complex morphology between Fig. 16p and r (~ 40 min after egress to ~ 2 h after egress). At 40 min post-eclipse, the atmosphere is still largely sustained by material desorbing from the non-frost surface. Yet one hour after eclipse, the frost surface has warmed to the point where it contributes a substantial amount to the dayside column densities. For the next hour, the SO_2 gas desorbing from the non-frost surface is condensing on the nearby SO_2 frosts and is being replaced by gas sublimated from the frost surface. Two hours after eclipse, the peak T_F has recovered within 1.5 K as discussed in Section 3.1.3. Even at the end of the simulation (~ 2 h post-eclipse), however, the effect of eclipse on the atmosphere persists.

3.2.2. Global winds

The day-to-night pressure gradient driven by the variation in insolation absorbed by the surface drives SO_2 winds that have net sublimation from the region near the peak T_F and net condensation on and near the nightside. Outside of eclipse, the day-to-night pressure gradient is strong enough to drive the winds substantially supersonic (the Mach number, $M > 2.0$) in certain regions of the atmosphere (generally near the terminator and outside of the surface boundary layer). The flow structure nominally consists of flow originating at the peak pressure region (centered at the location of the peak T_F) and diverging in all directions toward the nightside. An oblique shock forms near the dawn terminator as supersonic SO_2 gas condenses on and near the nightside. At 10 km, the peak wind speed is ~ 500 m/s and increases to ~ 575 m/s at 40 km. Note wind speeds are relative to the underlying surface not an Earth-based observer.

An east/west asymmetry does exist due to the gas-surface interaction that creates the DAE. The DAE is a high pressure region which acts as an obstruction to the global winds that flow west

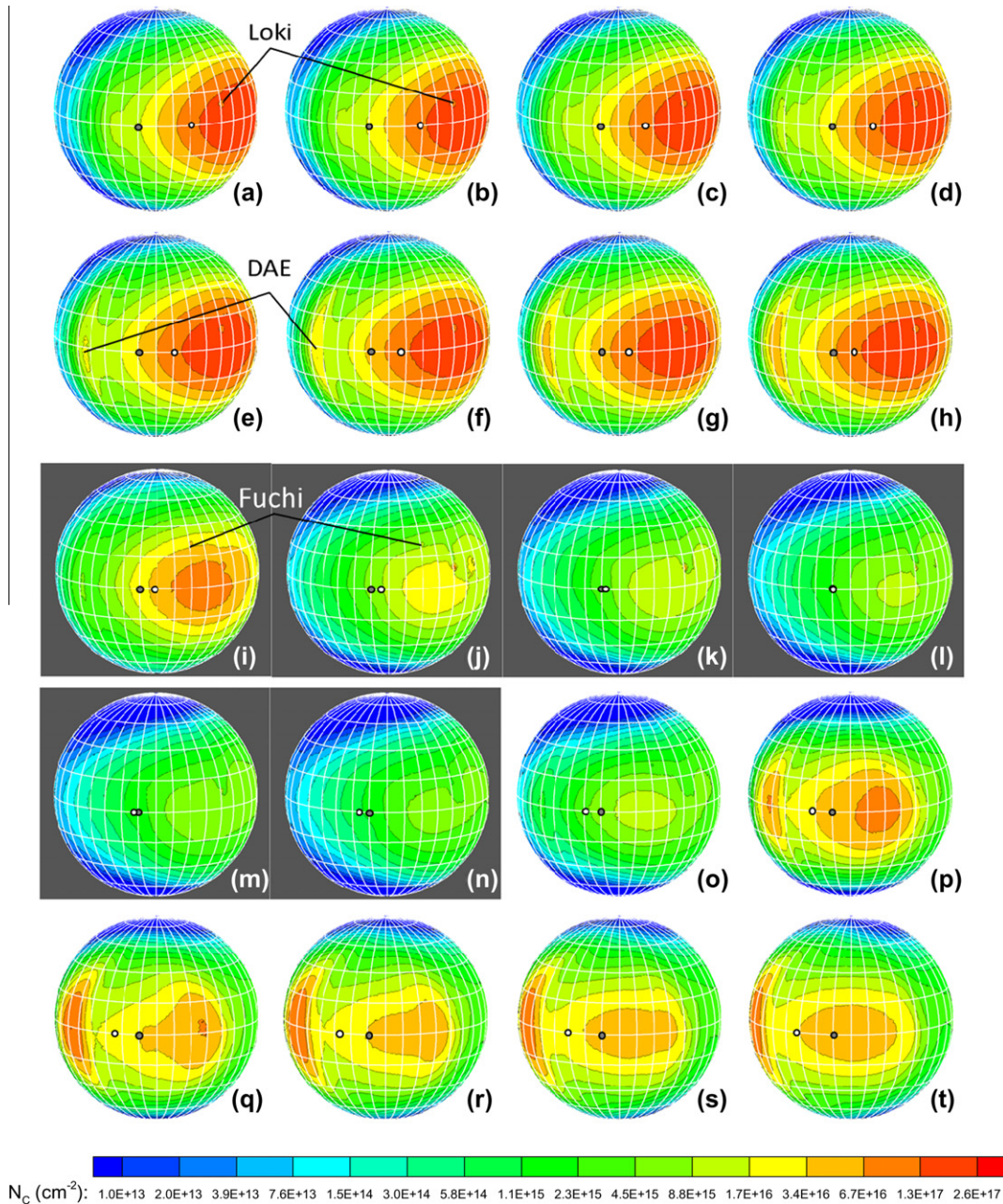


Fig. 16. (a–t) Column density contours with the view centered at (10°N, 350°W) as a function of time. The 20 snapshots occur at intervals of 1250 s (~21 min) starting approximately 2 h and 40 min prior to eclipse and ending ~2 h after egress from eclipse. Hot spots, Loki (310°W, 10°N) and Fuchi (328°W, 25°N), are highlighted in (a) and (b) and (i) and (j), respectively. Loki is visible throughout the simulated time due to its large area whereas Fuchi is visible for only a short time at the beginning of eclipse because of its relatively smaller area. The white dot denotes the location of the subsolar point while the black dot denotes the location of the sub-jovian point. See the animation of this figure in the [Supplementary material](#).

from the region of peak pressure. Unsteadiness in the DAE leads to differing flow patterns throughout the simulation time. Prior to eclipse, the DAE is largely growing as the atmosphere approaches ingress and therefore the streamlines which are initially supersonic to the west start to be deflected by the high pressure DAE. Winds that are a significant distance from the equator (latitudes of $\pm 10^\circ$ or more) will deflect to the north or south whereas those nearer the equator will be forced up and over the high pressure region since that is the path of least resistance. In comparison, the eastward flow continues on much further than the westward flow due to the high Γ_F . The SO₂ frost surface cools very slowly leading to a “finger” of higher pressure extending far onto the nightside. At

40 km altitude, the pressure slowly decreases and the atmosphere is still partially collisional (mean free path ~ 20 km < lateral cell size of 30 km) after passing through $\sim 140^\circ$ (or 16 h) of night. Because T_F and therefore P decrease slowly east of dusk, the winds in these regions deflect north or south due to the relatively cold mid-latitudes (<90 K) and poles (~ 55 K).

When the flow becomes only marginally collisional, bordering on free molecular, streamlines can be deceptive. For example, two inter-penetrating non-collisional streams of gas may be interpreted by a streamline tracing program as producing a stagnation flow due to the superposition of their bulk velocities when no such stagnation flow structure exists. We have been careful here only

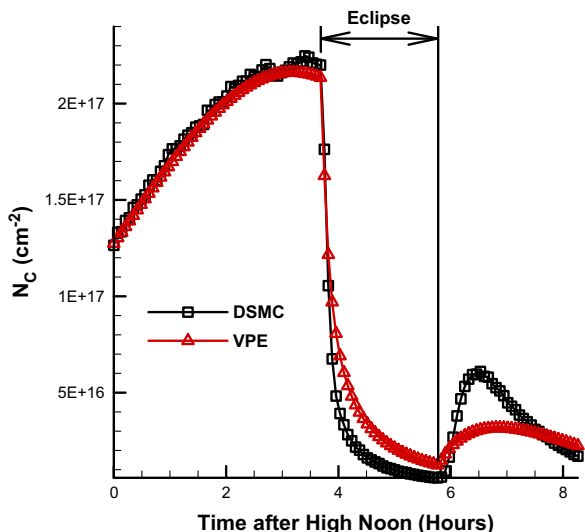


Fig. 17. A comparison of the VPE and DSMC computed column densities at (0°N , 315°W). Contrary to expectations based on one-dimensional eclipse observations with uniform frost coverage (Moore et al., 2009), the VPE column density collapses slower than the DSMC computed column density because VPE neglects absorption onto and desorption from the non-frost surface. As the non-frost surface cools rapidly, that portion of the atmosphere will collapse leaving a diminishing portion of the atmosphere sustained by sublimation from the frost surface.

draw conclusions on the global dynamics in regions where the streamlines are collisional and therefore, where streamlines are physically meaningful.

As the atmosphere enters eclipse, the column collapses reducing the day-to-night pressure gradient that drives the global winds. Early in eclipse, the pressure gradient is still strong enough to drive the flow supersonic near the terminator but as the atmosphere continues to collapse, the pressure gradient is reduced to the point where the flow is subsonic everywhere and the oblique shock near the dawn terminator disappears. Prior to eclipse, the peak near surface (~ 1 km altitude) pressure is ~ 3 nb whereas the peak pressure has dropped to ~ 80 pb just before egress from eclipse. As discussed earlier in Section 3.1.3, the peak T_F point has a prograde rotation during eclipse leading to the region of peak pressure also moving in the prograde direction. Since the peak pressure always acts as the origin of the flow, this leads to a prograde rotation of the point of origin for the global winds as the atmosphere approaches egress. Furthermore, eclipse tends to “flatten” the temperature distribution leading to a much more uniform T_F around Io; therefore, the contribution of the inhomogeneous frost fraction becomes more significant in the absence temperature gradients. Late in eclipse, the inhomogeneous frost fraction leads to the separation of the peak pressure into two equally strong but independent high pressure regions. These two regions both act as sources for global winds leading to a small region of stagnated gas between them.

Upon egress from eclipse (see Fig. 18o), the surface warms and the dayside pressure once again rises while the nightside pressures remain constant. As discussed in Section 3.2.1, the excess SO_2 gas that condenses on the non-frost surface during eclipse rapidly desorbs upon egress from eclipse. Initially, this causes the atmosphere to be primarily supported by the non-frost surface and therefore the atmosphere has only a $\sim 11^{\circ}$ eastern lag between its peak column density and the subsolar point. This in turn causes the circumplanetary flow to originate $\sim 11^{\circ}$ east of the subsolar point as opposed to the usual $\sim 33^{\circ}$ eastern lag. The day-to-night pressure gradient remains fairly weak (subsonic) because of the relatively low pressure atmosphere supported by the non-frost surface. Approximately 1 h after egress from eclipse, the atmosphere

establishes a two peak structure (for a second time but due to a different mechanism; see Fig. 18q) as discussed in Section 3.2.1. Each of these high pressure regions forces flow away toward low pressure regions and the pressure gradient is strong enough to drive some flow supersonic near the terminator. Because the two high pressure regions (seen in Fig. 18p–t) are roughly equal strength, the two opposing winds form a stagnation flow pattern. The stagnation flow forms roughly $2/3$ the distance from the peak pressure to the DAE because the winds from the peak pressure are stronger. Winds that are primarily east/west near the equator are forced north and south. This flow pattern continues to the end of the simulation. Note that the apparently very high/low Mach numbers near the poles ($>75^{\circ}\text{N/S}$) are due to poor simulation statistics where the equilibrium vapor pressure has fallen to $\sim 10^{-10}$ or less of the peak vapor pressure; they are not physically meaningful.

Millimeter range observations (Moulet et al., 2008) measured a 330 ± 100 m/s limb-to-limb velocity on the leading hemisphere. The measurements indicated super-rotating circumplanetary winds in the prograde direction. Although the simulations presented here are of the sub-jovian hemisphere (centered at 0°W), a tentative comparison to the millimeter range observations (Moulet et al., 2008) can be made of the leading hemisphere (90°W). The simulated wind patterns do not recreate the observed super-rotating prograde winds. Simulated wind speeds near the dusk terminator have wind speeds of ~ 500 m/s in the prograde direction at 10 km but this must be integrated in altitude to determine the wind speeds of the bulk atmosphere because the density is falling off exponentially with altitude. The integrated equatorial wind speeds along the dusk terminator are ~ 150 m/s in the prograde direction. Simulated equatorial wind speeds integrated with altitude near the dawn terminator are slower (~ 100 m/s) but are in the retrograde direction. Both these simulated wind speeds are given in Io’s frame of reference which must be transformed to match the observations which include Io’s ~ 75 m/s equatorial rotation rate. The simulated wind speeds in the frame of reference of the observations are ~ 225 m/s in the prograde direction near the dusk terminator and ~ 25 m/s in the retrograde direction near the dawn terminator. Recent simulations that include the momentum flux from energetic ions originating in the jovian plasma torus indicate that the plasma pressure can exert a large force on the circumplanetary winds (Moore, 2011). It may be that the observed super-rotating prograde winds (Moulet et al., 2008) are due to the relative orientation of the sub-plasma point and the subsolar point at eastern elongation. In that geometry, the plasma pressure would counteract the day-to-night pressure gradient that currently drives the simulated wind patterns.

3.2.3. Vertical atmospheric structure

To this point, only lateral gradients in the atmosphere have been discussed but there are significant vertical gradients in Io’s atmosphere due to gravity. Just prior to eclipse, the atmosphere falls off exponentially with altitude and the gas density, n , is $\sim 2.8 \times 10^{17} \text{ m}^{-3}$ just above the surface near the peak pressure (see Fig. 19). The scale height, $H = k_B T / mg$, is ~ 8.6 km near the surface but generally increases with altitude due to plasma heating (e.g. at 100 km altitude, $n \sim 1.3 \times 10^{14} \text{ m}^{-3}$ and $H \sim 36$ km due to the plasma heated gas reaching temperatures near 500 K and reduced gravity). The only exception to this temperature trend is near ~ 5 km altitude where a thermal inversion layer exists because the plasma energy that is traveling radially downward through the column of gas is completely absorbed above that point. Below ~ 5 km altitude, the subliming SO_2 gas expands upwards adiabatically and cools radiatively, while above ~ 5 km altitude, the gas is heated by the plasma energy flux.

After 10 min in eclipse, the peak n near the surface decreases to $\sim 1.6 \times 10^{16} \text{ m}^{-3}$ ($\sim 5.7\%$ of the pre-eclipse number density; see

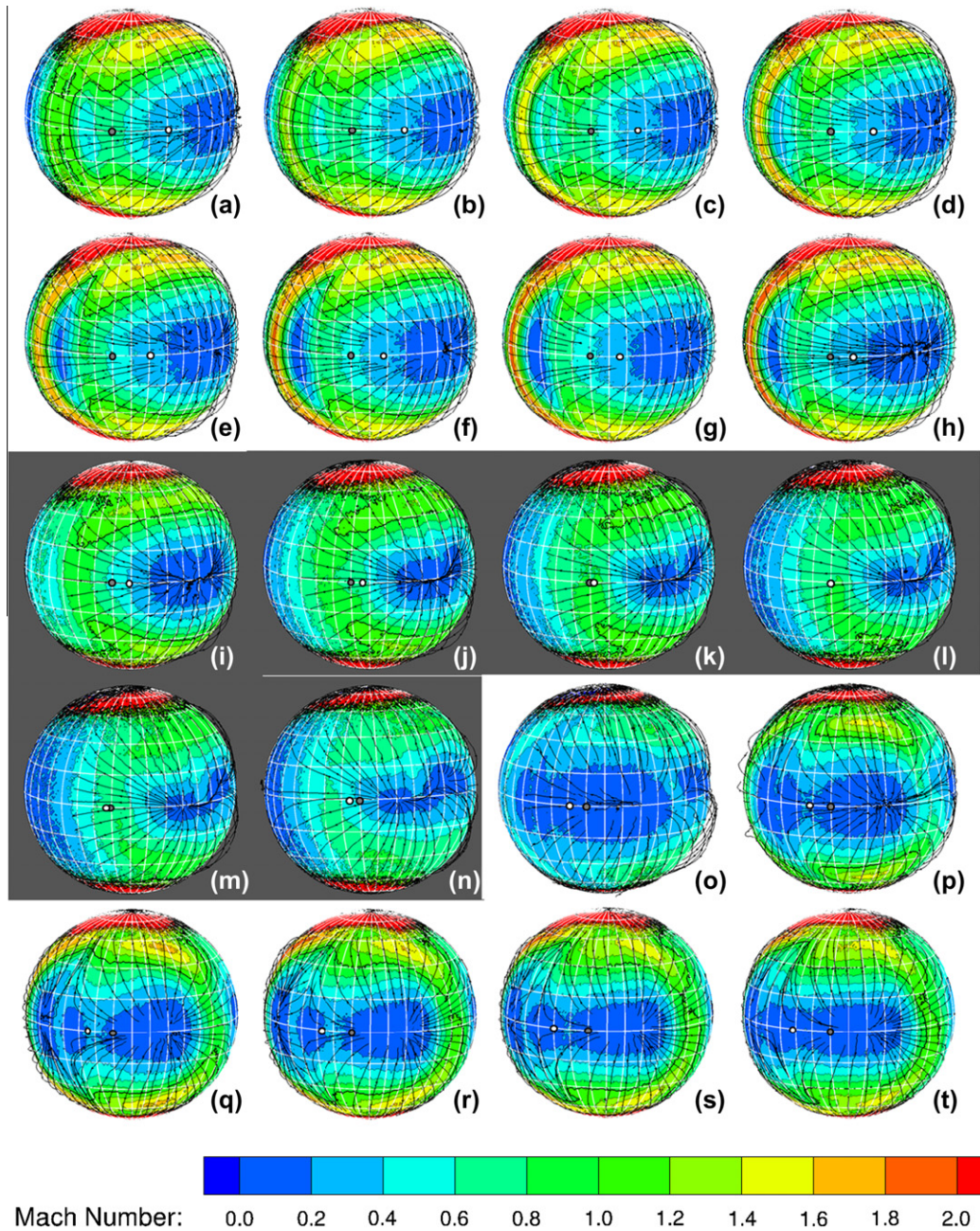


Fig. 18. Mach number contours overlaid with streamlines with the view centered at (0°N , 10°W) as a function of time. The 20 snapshots occur at intervals of 1250 s (~ 21 min) starting approximately 2 h and 40 min prior to eclipse and ending ~ 2 h after egress from eclipse. The white dot denotes the location of the subsolar point while the black dot denotes the location of the sub-jovian point. See the animation of this figure in the Supplementary material.

Fig. 19). After ~ 100 min in eclipse, the atmosphere has further collapsed to $n_{\text{PEAK}} \sim 4.4 \times 10^{15} \text{ m}^{-3}$ ($\sim 1.6\%$ of the pre-eclipse number density). Twenty minutes after egress from eclipse, n_{PEAK} rapidly increases to $\sim 1.0 \times 10^{17} \text{ m}^{-3}$ ($\sim 35.7\%$ of the pre-eclipse number density). Two hours after egress from eclipse, the n_{PEAK} has slightly decreased to $\sim 6.5 \times 10^{16} \text{ m}^{-3}$ ($\sim 23.5\%$ of the pre-eclipse number density). The overshoot in n_{PEAK} just after egress from eclipse is caused by the excess SO_2 condensed on the non-frost surface during eclipse that rapidly desorbs and inflates the atmosphere. Two hours after egress from eclipse, most of the excess SO_2 has already desorbed from the non-frost surface leaving sublimation from SO_2 surface frosts as the primary support for the atmosphere. At high altitudes, n follows the trend of the near surface value and the only major departure is just before egress from eclipse (~ 100 min into

eclipse) where n is roughly five times lower than the pre-eclipse values above 20 km altitude.

The vertical thermal profile also undergoes morphological changes during eclipse. Prior to eclipse, there is a thermal inversion layer near the surface in the subsolar region due to the depletion of incoming plasma energy above ~ 5 km altitude. As the atmosphere collapses in eclipse, the column density becomes thin enough that plasma energy reaches all the way to the surface. After ~ 10 min in eclipse, the inversion layer has disappeared and the gas translational temperature, T_{TRANS} , at 1 km altitude has increased slightly (~ 140 K) due to plasma heating. Near the end of eclipse (~ 100 min into eclipse), T_{TRANS} at 1 km altitude has increased further (~ 160 K) because the thinner column allows more plasma energy to reach near the surface. Upon egress from eclipse, the

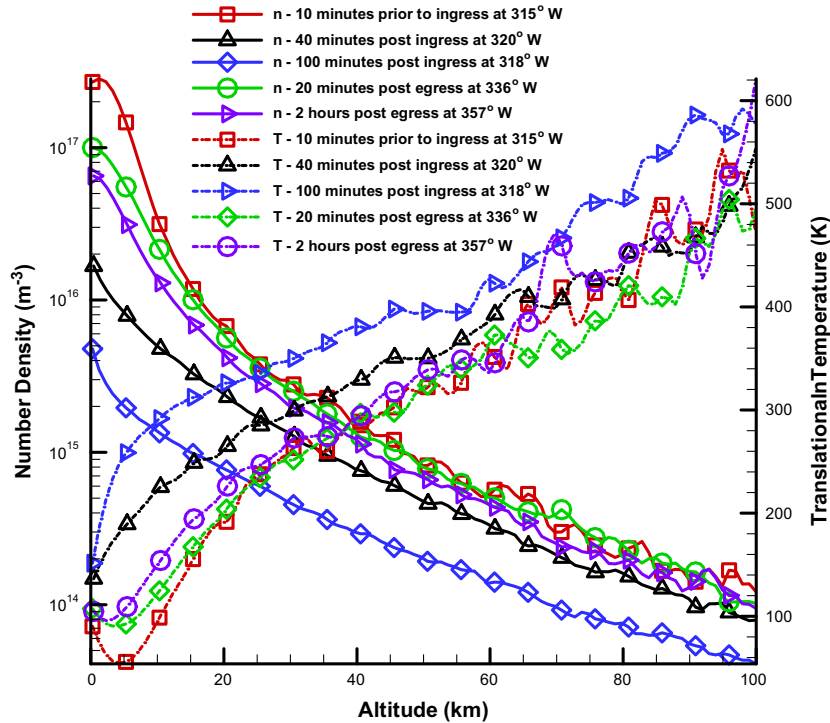


Fig. 19. Number density (solid lines) and translational temperature (dash-dot lines) as a function of altitude at the instantaneous location of the peak equatorial pressure. Data are shown at the following times: ~ 10 min prior to eclipse (0°N , 315°W), ~ 40 min post ingress (0°N , 320°W), ~ 100 min post ingress (0°N , 318°W), ~ 10 min after egress (0°N , 336°W), and ~ 2 h after egress from eclipse (0°N , 357°W).

atmosphere thickens and the inversion layer is rapidly reestablished. Within ~ 20 min after egress from eclipse, an inversion layer has re-formed but subsequently weakens ~ 2 h after egress from eclipse because of the thinner atmosphere at that time. At higher altitudes, the atmosphere is warmed by the plasma heating. T_{TRANS} increases nearly linearly with altitude above ~ 20 km before, during, and after eclipse. With the present model, plasma heating leads to temperatures in excess of 500 K at high altitudes. In Fig. 19, the vertical profile of the atmosphere at the instantaneous location of the peak pressure (as it moves in time) was investigated. In Fig. 20, the atmosphere is instead sliced along the equator to show the atmospheric structure as a function of both altitude and longitude.

Ten minutes prior to eclipse, the atmosphere is largely supported by sublimation from SO_2 surface frosts rather than desorption from the non-frost surface. The only exception is near 40°W where the DAE forms (see Fig. 20a). Note that the DAE occurs at a local time of $\sim 8:40$ AM and the dawn terminator occurs at 6:00 AM. The gas density, n , slowly decreases just east of dusk (280 – 285°W) whereas there is an abrupt drop-off in n just west of dawn (75 – 80°W) due to the high thermal inertia of the SO_2 surface frosts. The dayside exobase (the altitude at which the SO_2 gas mean free path is equal to the atmospheric scale height) peaks at ~ 180 km altitude; from dusk, this exobase altitude decreases linearly with decreasing longitude to ~ 110 km altitude at the anti-jovian point (180°W). The exobase reaches a minimum of ~ 25 km altitude at 80°W .

Forty minutes into eclipse, the atmosphere has collapsed significantly but the dayside exobase between 270°W and 360°W remains at ~ 180 km altitude (see Fig. 20b). The exobase height in that region remains relatively unchanged for two reasons: (i) the collapse is partially limited by the speed of sound and, more importantly, (ii) Γ_F is large leading to slow changes in T_F . The nightside exobase remains unchanged because the transport of mass from the dayside to nightside by circumplanetary flow is

small and changes in flux do not have time to develop. The primary changes to the exobase height occur between 0°W and 90°W . The atmosphere above the DAE (40°W) is most strongly affected because it had been supported by the non-frost surface which has a low Γ_{NF} which means T_{NF} decreases rapidly during eclipse. Therefore, the DAE disappears and the exobase drops to ~ 60 km altitude. The exobase near dawn (90°W) drops nearly to the surface (only ~ 10 km altitude).

One hundred minutes into eclipse, the atmosphere has collapsed further and the dayside exobase between 270°W and 360°W descends to ~ 160 km due to further thinning of the atmosphere (see Fig. 20c). The exobase near dawn ($\sim 60^\circ\text{W}$) ultimately drops to ~ 7.5 km while the nightside exobase altitudes remain fairly constant. Note that the exobase at a given longitude on the nightside will decrease in time because the atmosphere has been in night longer.

Twenty minutes after egress from eclipse, the peak exobase has recovered to ~ 160 – 200 km altitude on the dayside and the minimum exobase altitude has increased from ~ 7.5 km to ~ 25 km (see Fig. 20d). Two hours after egress from eclipse, the exobase looks fairly similar to the morphology 20 min after egress but the minimum has increased to ~ 50 km (see Fig. 20e). The reason for this increase in the minimum exobase altitude is that the location of the minimum is now on the anti-jovian hemisphere which has slightly warmer surface temperatures since it never experiences eclipse.

The translational temperature just prior to eclipse seen in Fig. 21a has a morphology similar to that found in Walker et al. (2010). On the dayside, the gas at low altitudes is relatively cold (< 120 K) because the overlying atmosphere is thick enough to absorb all of the plasma energy above these altitudes. The plasma energy depletion creates a “dome” of cold gas below which the gas does not experience any plasma heating. The DAE near 40°W is also visible since it becomes thick enough to create a small pocket of cold gas near the surface. Near the dawn terminator, a high

temperature ($T_{TRANS} > 1000$ K) region exists due to compressional shock heating as circumplanetary flow condenses on and near the nightside. At 40 km altitude in the region where the oblique shock is forming, the atmosphere is rarefied (the mean free path

is between 10 km and 70 km), and the shock itself is also thick spanning over 700 km. The shock thickness increases with altitude as the atmosphere becomes more rarefied. Near the surface, the mean free path decreases to ~ 4 km but this is in the boundary

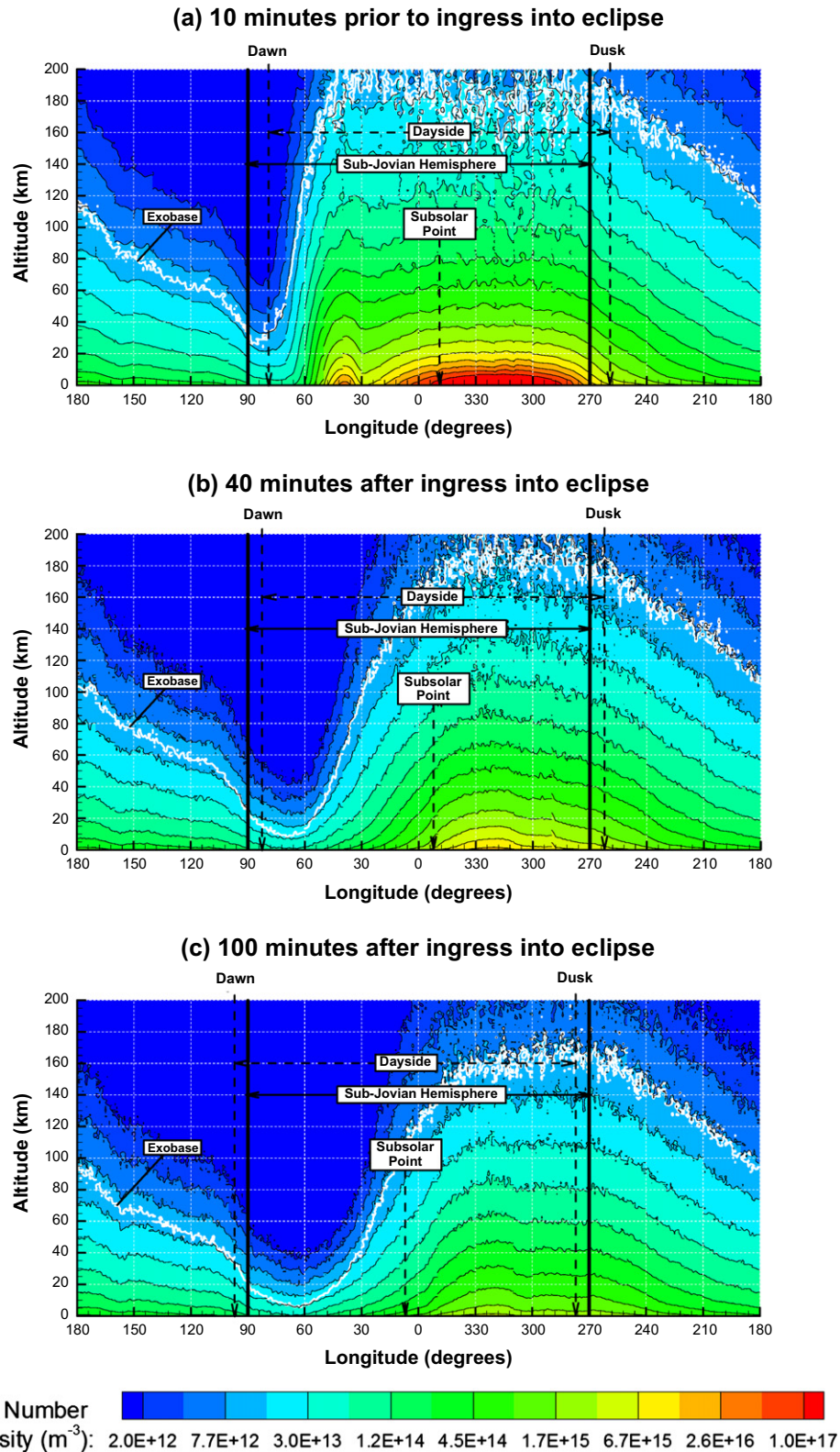
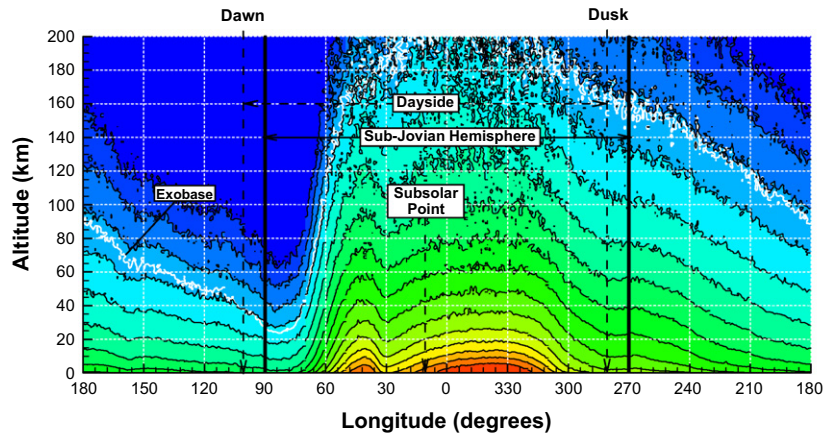


Fig. 20. Contours of number density as a function of altitude and longitude for five instances near eclipse: ~ 10 min prior to eclipse, ~ 40 min after ingress into eclipse, ~ 100 min after ingress into eclipse, ~ 20 min after egress from eclipse, and ~ 2 h after egress from eclipse. The location of the exobase is denoted by a white line. See the animation of this figure in the Supplementary material.

(d) 20 minutes after egress from eclipse



(e) 2 hours after egress from eclipse

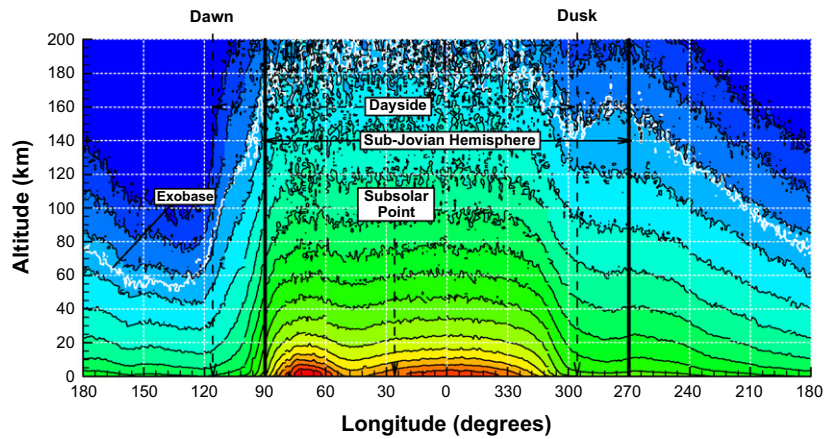


Fig. 20 (continued)

layer of the flow. Although the shock looks nearly normal in Fig. 21a and e, this is due to the aspect ratio of the figures which are severely distorted. Each degree of longitude is equal to ~ 30 km, so the x -axis is compressed by a factor of ~ 26.7 compared to the y -axis. Therefore, despite the shock appearing normal, it is actually highly oblique.

At high altitudes (>100 km), the dayside translational temperatures become noisy because the number of computational molecules in each column of cells is constrained to be the same (1000 molecules) and the distribution is biased towards lower altitudes. On the nightside, the statistics are better at higher altitudes because the scale height is larger due to plasma energy reaching the surface and heating the atmosphere (compare altitudes between 180 and 200 km in dayside area between 300°W and 330°W with the nightside, especially between 150° and 210°W , in Fig. 21a).

Forty minutes *after entry* into eclipse, the collapse of the atmosphere allows plasma energy to penetrate to much lower altitudes and the atmosphere is significantly warmer on the dayside (see Fig. 21b). At 1 km altitude, the atmosphere over the peak pressure region warms to ~ 140 K due to the plasma heating. The atmosphere near the DAE collapses rapidly and the “pocket” of cold gas that existed due to the depletion of plasma energy is replaced

by warmer gas through which plasma is able to reach to the surface. At high altitudes between 60° and 90°W (where the oblique shock existed), the shock rapidly dissipates due to the decreased day-to-night pressure gradient. At high altitudes, the data become very noisy due to the extremely low densities ($<10^{10} \text{ m}^{-3}$). This is especially true between 70°W and 100°W where the average number of molecules per cell drops below two, resulting in misleading contours. Some residual hot gas (>800 K) still exists but is likely not due to compressional shock heating. The thermal structure of the atmosphere on the nightside remains very similar to the pre-eclipse structure.

Approximately 100 min *after* ingress into eclipse, the atmosphere has collapsed further and plasma energy is able to warm to the gas near the surface (1 km altitude) to ~ 160 K (see Fig. 21c). Gas at the surface remains in thermal equilibrium at ~ 111 K. The location where the oblique shock existed prior to eclipse has dropped to extremely low densities as the day-to-night pressure gradient further decreases. The nightside thermal structure largely remains the same with slight cooling at high altitudes.

Twenty minutes *after egress* from eclipse, the non-frost surface has warmed significantly because of its low Γ_{NF} (see Fig. 21d). The material that condensed on the cold (~ 90 K) non-frost surface

during eclipse rapidly desorbs as the non-frost surface warms and the sublimation atmosphere gradually thickens. This causes the “dome” of cold gas on the dayside to reappear. Although the

atmospheric column density has begun to increase in the 10 min after eclipse, the timescale on which the circumplanetary flow equilibrates is much longer. This timescale is controlled by the

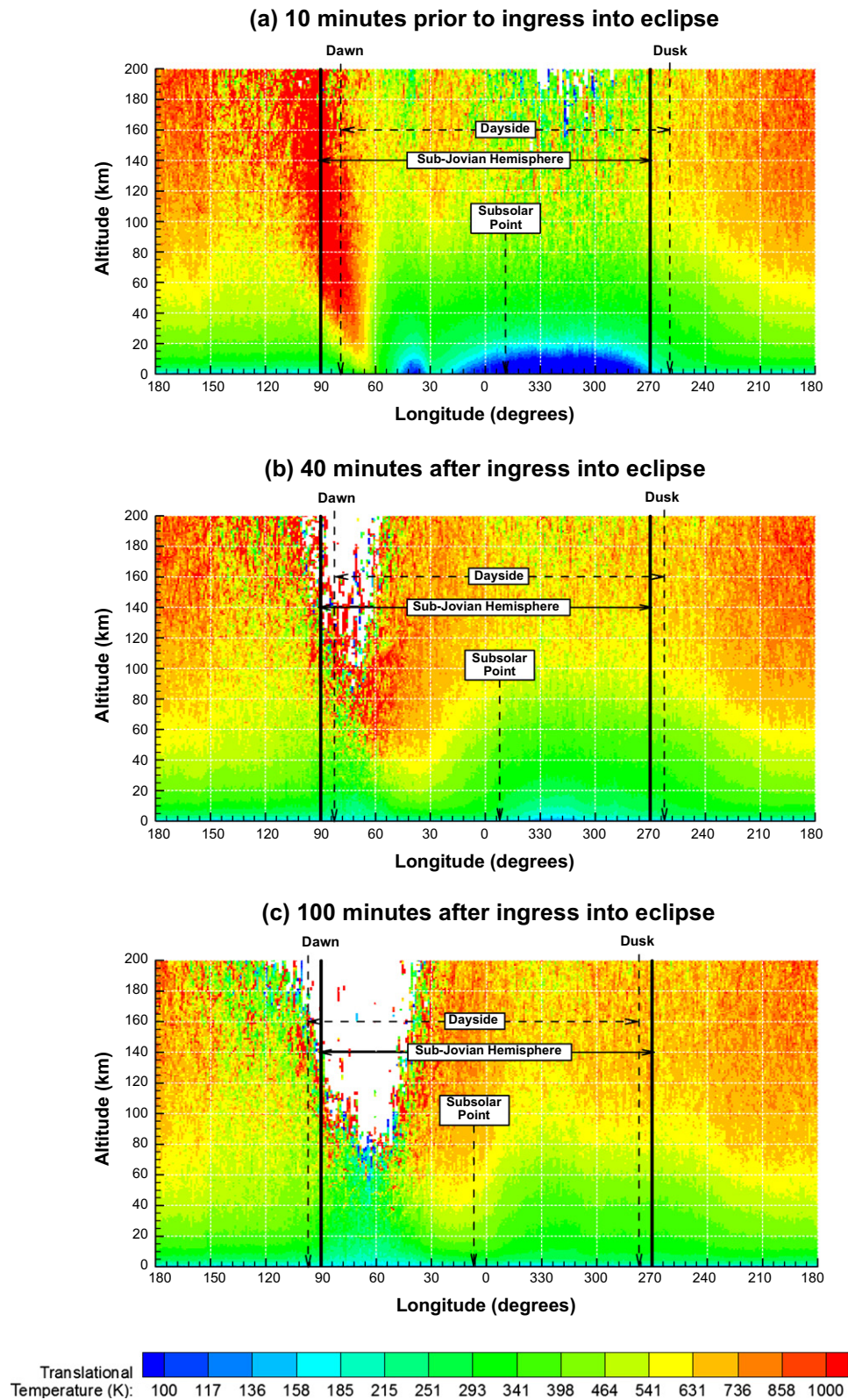
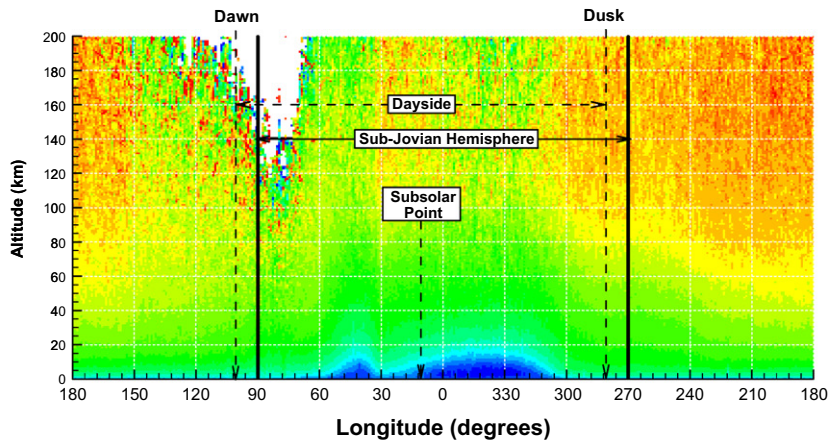


Fig. 21. Contours of translational temperature as a function of altitude and longitude for five times near eclipse: ~ 10 min prior to eclipse, ~ 40 min after ingress into eclipse, ~ 100 min after ingress into eclipse, ~ 20 min after egress from eclipse, and ~ 2 h after egress from eclipse. Values are blanked where the $T_{\text{TRANS}} < 30$ K due to insufficient statistics. The final image shows the compressional heating near the shock at the correct aspect ratio for the case (a) ~ 10 min prior to eclipse. See the animation of this figure in the Supplementary material.

(d) 20 minutes after egress from eclipse



(e) 2 hours after egress from eclipse

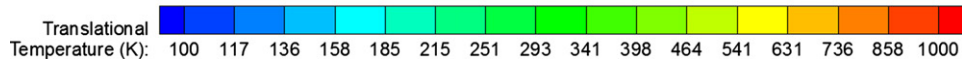
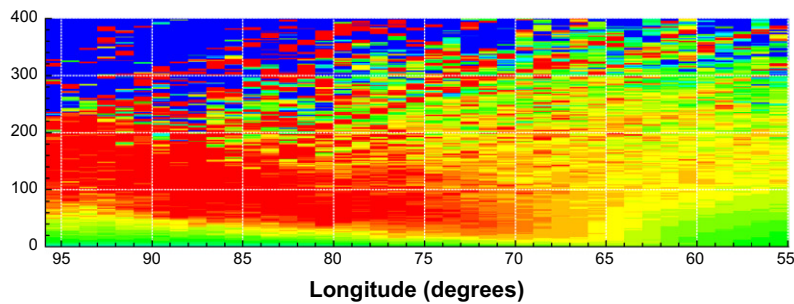
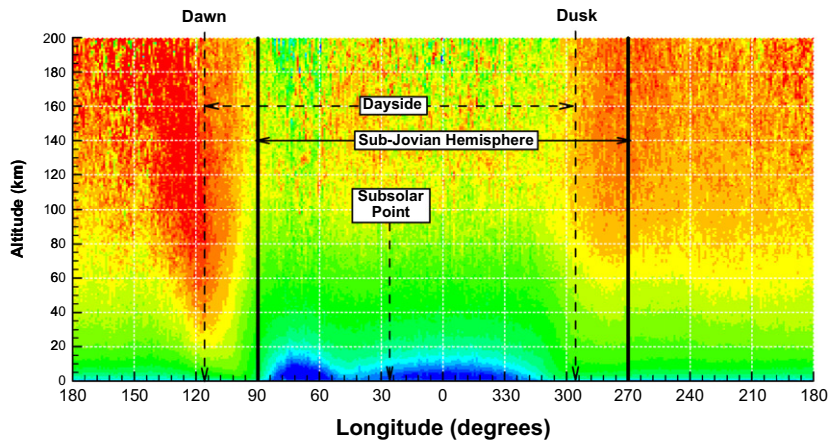


Fig. 21 (continued)

speed of sound, a_{GAS} , and the distance the gas must travel, d_C . It will vary with altitude but a rough estimate of the timescale at 40 km altitude is $t_C = d_C/a_{GAS} \approx 3$ h assuming $T_{TRANS} \approx 400$ K and $d_C \approx 2800$ km (a quarter of Io's circumference). Therefore, the compressional heating from the oblique shock is absent because the SO_2 gas flow is still predominantly subsonic. The DAE is visible from the cold "pocket" of gas that it creates at $\sim 45^\circ W$. Noisy conditions exist at high altitudes (>100 km) where the oblique shock existed prior to eclipse.

Two hours *after* egress from eclipse, the atmosphere has nearly recovered from eclipse and the T_{TRANS} morphology is similar to the atmosphere 10 min prior to ingress (see Fig. 21e). The day-to-night

pressure gradient is large enough to drive the flow supersonic and the oblique shock near the dawn terminator reappears. The atmosphere over much of the dayside remains thick enough to deplete the plasma energy before it reaches the surface leaving cold gas near the surface. The relative sizes of the cool gas "pockets" formed by the DAE and the peak pressure region change as a function of time. Comparing Fig. 21e to a, the DAE has grown in size while the peak pressure region has not yet fully recovered from eclipse because of the high thermal inertia of the frost surface (see Section 3.1.3).

Moulet et al. (2008) measured mean gas temperatures between 130 and 180 K and Spencer et al. (2005) inferred a gas temperature less than 150 K. Both observations agree with our column

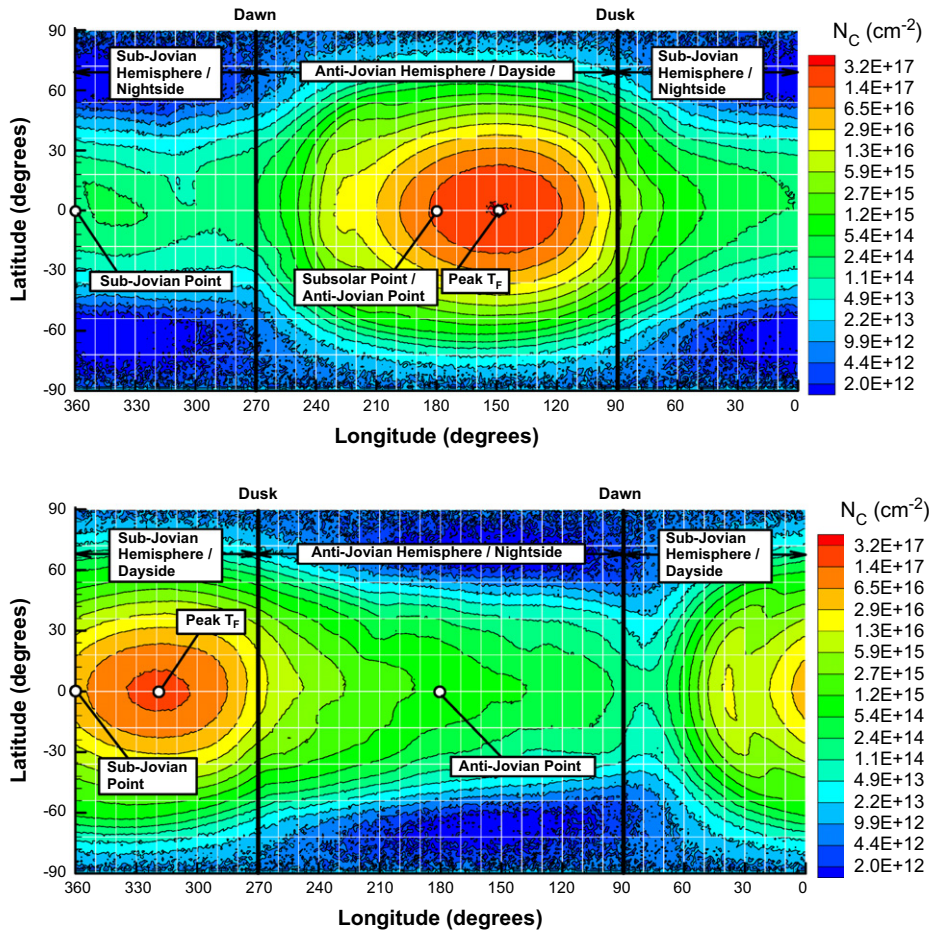


Fig. 22. A comparison between the anti-jovian dayside atmosphere and the sub-jovian dayside atmosphere (at an instant just before ingress into eclipse). The anti-jovian hemisphere has higher column densities throughout because of the higher underlying T_F .

integrated SO_2 gas temperatures which range between 90 and 200 K on the dayside hemisphere. The lower values occur nearer the peak T_F where the bulk of the atmosphere remains cold due to plasma depletion. Higher column integrated translational temperatures occur near the terminator where plasma penetrates the entire column of gas.

3.2.4. Anti-jovian vs. sub-jovian hemisphere

The effects of eclipse on the atmosphere are finally examined by comparing the sub-jovian atmosphere prior to eclipse with the anti-jovian hemisphere. Column densities on the anti-jovian hemisphere's dayside are higher than for the sub-jovian hemisphere and the anti-jovian hemisphere's peak dayside SO_2 gas column density, N_C ($\sim 3.2 \times 10^{17} \text{ cm}^{-2}$) is $\sim 45\%$ higher than the sub-jovian hemisphere's peak of $N_C \approx 2.2 \times 10^{17} \text{ cm}^{-2}$ (see Figs. 22 and 23). As seen in Fig. 22, the morphology of both atmospheres is similar with elliptic contours of column density centered around the peak T_F which in both cases lags the subsolar point by $\sim 33^\circ$. This 33° thermal lag means that the peak T_F lags the subsolar point by 3 h and 50 min (see Fig. 23). Both hemispheres have a long atmospheric "tail" that extends past dusk and onto the nightside. Nightside column densities for the case with the anti-jovian hemisphere on the dayside (such that the sub-jovian hemisphere is on the nightside) are slightly lower because of the lower underlying T_F due to eclipse's diurnally averaged effect. Both atmospheres have sharp gradients near the dawn terminator where the surface is just coming into sunlight.

To validate these atmospheric simulations, we compare to recent observations of Io's atmosphere. Feaga et al. (2009) used Lyman- α observations to illustrate a striking asymmetry between the sub-jovian and anti-jovian hemispheres of Io's atmosphere. In these observations, the anti-jovian hemisphere was found to have a higher average dayside column density than the sub-jovian hemisphere. They explained the asymmetry in terms of the distribution of volcanic centers where the anti-jovian hemisphere has a higher concentration of volcanoes. Our atmospheric simulations

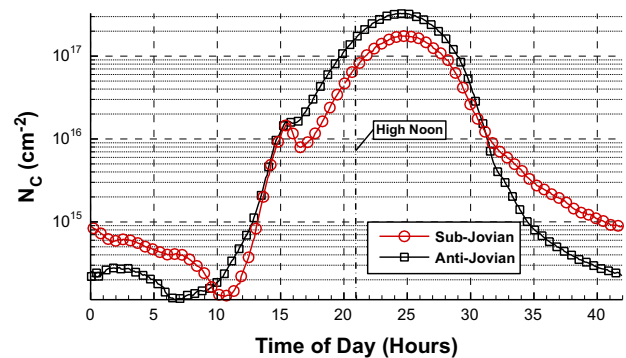


Fig. 23. Equatorial column densities for the anti-jovian and sub-jovian hemispheres plotted as a function of time of day such that "noon" occurs at the same point for each hemisphere. High noon occurs at 21 h. The DAE occurs at ~ 15 h.

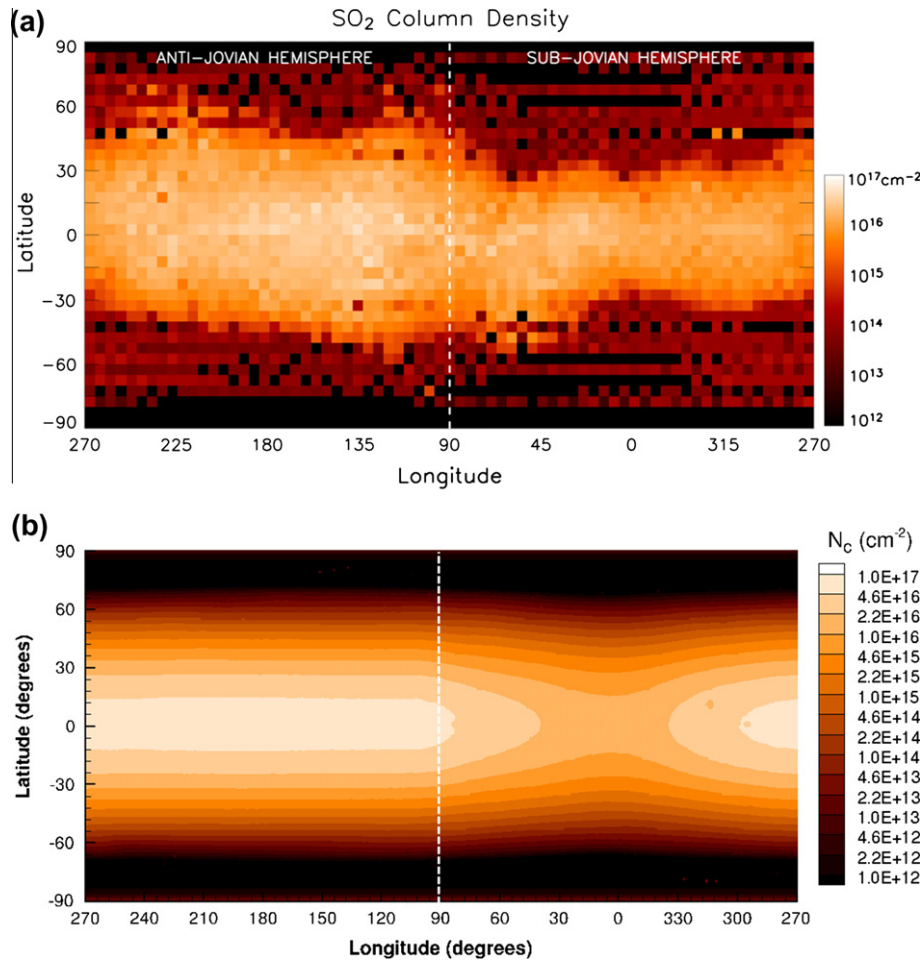


Fig. 24. (a) Observationally inferred (courtesy of Feaga et al., 2009) and (b) simulated “average dayside” SO_2 column densities. Both (a) and (b) show the anti-jovian hemisphere with higher “average dayside” column densities.

show that eclipse is an additional or alternative cause for the anti-jovian/sub-jovian asymmetry.

Unfortunately, to reconstruct Fig. 6 from Feaga et al. (2009) requires simulation of an entire Io orbit which is presently computationally prohibitive with a fully collisional atmosphere in DSMC. Instead, we simulate Io’s atmosphere in the absence of collisions (free molecular) for an entire orbit. This comparison is justified because the circumplanetary flow driven by molecular collisions does not significantly alter the column density from hydrostatic equilibrium. Forty “snapshots” of Io’s atmosphere were averaged to create an image of the “average dayside atmosphere”.

Fig. 24 compares the Lyman- α inferred “average dayside” column densities with our simulated (free molecular) column densities that include the effect of eclipse. Both show high “average dayside” column densities on the anti-jovian hemisphere. The simulated average dayside column densities on the anti-jovian hemisphere near the equator peak at $6.2\text{--}6.3 \times 10^{16} \text{ cm}^{-2}$. In comparison, the SO_2 column densities inferred from Lyman- α observations (Feaga et al., 2009) peak at $\sim 5 \times 10^{16} \text{ cm}^{-2}$ and generally range between 2 and $4 \times 10^{16} \text{ cm}^{-2}$ on the anti-jovian hemisphere. Simulated sub-jovian average dayside column densities are lower due to the effect of eclipse and reach an equatorial minimum at the sub-jovian point of $\sim 1.4 \times 10^{16} \text{ cm}^{-2}$. Simulated average dayside equatorial column densities gradually increase away from the sub-jovian point toward the anti-jovian hemisphere value. Again, the Lyman- α average dayside SO_2 column densities agree well with the simulated values and the equatorial values range from 1 to $2 \times 10^{16} \text{ cm}^{-2}$. This comparison may resolve the

apparent discrepancy between the SO_2 column densities observed in the Lyman- α (Feaga et al., 2009) and mid- to near-UV (Jessup et al., 2004). The simulation is much smoother than the observation and this could be due to the lack of volcanic plumes in our current model, observational noise, or the effect of the residence time of SO_2 gas on the non-frost surface which tends to smooth atmospheric column densities despite the underlying inhomogeneous SO_2 surface frosts. In our model, longer residence times would result in an aphysical build-up of SO_2 frost on the non-frost surface through multiple orbits; therefore, there must be another mechanism for denuding the non-frost surface of the thin layer of SO_2 that builds up during the night. We hypothesize that night time sputtering by high energy ions might keep the surface denuded (Moore et al., 2009).

4. Conclusions

A parametric study was performed to constrain the thermophysical parameters of Io’s surface. A modestly sophisticated thermal model was used to generate the thermal distributions that were compared to observational data in order to find the best fit thermophysical parameters via a least-squares error method. The thermal model solved the one-dimensional heat conduction equation with depth into Io’s surface and includes the effects of thermal inertia, latent heat of sublimation and condensation, eclipse by Jupiter, and the contribution of radiation from Jupiter. The thermal model solves the heat conduction equation for two separate surface

components: SO₂ frosts and non-frost (likely pyroclastic dusts and/or sulfur allotropes). A brute force search through the thermophysical parameters (albedo and thermal inertia) was performed and the resulting SO₂ surface frost temperature distribution was compared to the inferred frost temperatures of Jessup et al. (2004) assuming vapor pressure equilibrium. Because the assumption of vapor pressure equilibrium does not hold globally, a VPE correction factor was applied to account for non-equilibrium. The best fit thermophysical parameters for the SO₂ surface frost were found to be $\alpha_F \approx 0.55$ and $\Gamma_F \approx 200 \text{ J m}^{-2} \text{ K}^{-1} \text{ s}^{-1/2}$. With the best fit frost thermophysical parameters fixed, the non-frost thermal inertia was varied (α_{NF} was constrained by the mean albedo and mean frost fraction) and the resulting temperature distributions were compared to Galileo PPR observations of the surface brightness temperature (Rathbun et al., 2004). Again utilizing the least squares error method, the best fit non-frost thermophysical parameters were found to be $\alpha_{NF} \approx 0.49$ and $\Gamma_{NF} \approx 20 \text{ J m}^{-2} \text{ K}^{-1} \text{ s}^{-1/2}$. These thermophysical parameters can help interpret the state of the two surface components. The high Γ_F indicates that the SO₂ surface frosts have likely annealed due to the temperature variation between day and night (Sandford and Allamandola, 1993). Meanwhile, the low Γ_{NF} indicates that the non-frost surface is likely highly porous and composed of fine grained particulates.

After constraining the thermophysical parameters, they were used to generate the solid surface boundary condition in DSMC atmospheric simulations. The atmospheric simulations focused on the effect of eclipse on the atmospheric winds, temperatures, and densities. Results presented span approximately 6 h of Io's 42 h orbit with eclipse occurring near the middle of the simulated time and also include a single snapshot of the anti-jovian dayside atmosphere. We found that eclipse causes significant variations in the atmospheric morphology of the sub-jovian hemisphere. The DSMC atmospheric simulations with the best fit thermophysical parameters show that the majority of Io's atmosphere away from active volcanic centers can be fit by a purely sublimation-driven atmosphere.

The SO₂ surface frosts have a high thermal inertia leading to a $\sim 5 \text{ K}$ drop in T_F during eclipse; however, this corresponds to a factor of 20 decrease in column density due to the exponential dependence of the SO₂ vapor pressure on T_F . The dayside atmosphere on the sub-jovian hemisphere becomes thin enough during eclipse that plasma is able to reach to the surface thereby changing the vertical thermal structure. Supersonic circumplanetary flow exists prior to eclipse but becomes subsonic during eclipse because the day-to-night pressure gradient weakens considerably as the surface cools and atmosphere condenses. Before eclipse, an oblique shock exists near the dawn terminator where the supersonic flow condenses on and near the cold nightside. During eclipse, the oblique shock disappears as the day-to-night pressure gradient weakens. The thermal model predicts a prograde displacement of the atmosphere during eclipse (as opposed to the retrograde displacement that exists outside of eclipse) due to the differing amounts of insolation absorbed by the surface due to eclipse. After egress from eclipse, both the SO₂ surface frost and non-frost surface warm (but at different rates based on their respective thermophysical parameters). The atmosphere begins to recover from eclipse and slowly converges to the pre-eclipse quasi-steady state. The timescale for recovery of the surface temperature distribution to the pre-eclipse quasi-steady state is primarily controlled by the thermal parameter, θ , defined in Section 3.2 (Spencer et al., 1989). This "thermal parameter" was calculated to be $\theta_F \approx 14.9$ with the best fit thermophysical parameters. The circumplanetary winds respond over a different timescale ($\sim 2 \text{ h}$) controlled by the speed of sound. Because an excess of SO₂ gas condenses on the cold non-frost surface during eclipse, the post-eclipse DAE becomes comparable in pressure to the peak pressure region ($\sim 30^\circ$ east of the subsolar point).

The pressure gradients away from these two high pressure regions drive opposing flows which meet and form a stagnation point flow.

Lastly, the DSMC simulated atmospheres of sub-jovian and anti-jovian hemispheres are compared. Eclipse may partially account for the asymmetry observed in the Lyman- α (Feaga et al., 2009; Tsang et al., 2012). A composite "average dayside atmosphere" is created by simulating an entire Io orbit in the absence of molecular collisions and then averaging the atmosphere at 40 equal intervals throughout the orbit. There are lower sub-jovian column densities but the simulation finds much smoother contours than the Lyman- α observations. The differences could be due to interaction of SO₂ gas with the non-frost surface which tends to smooth SO₂ column densities over inhomogeneous frosts or the absence of volcanic plumes in our simulations. The column densities from the simulated average dayside atmosphere agree in magnitude with those inferred from Lyman- α observations (Feaga et al., 2009) despite the simulation's surface temperatures being fit to mid- to near UV observations (Jessup et al., 2004) that indicate much higher instantaneous column densities than the Lyman- α observations. Future work will explore the impact of a sophisticated plasma model that includes the effects of the electric and magnetic fields on the plasma, as well as sputtering and chemistry caused by high energy ions in the plasma torus. Moore (2011) studied these effects on Io's atmosphere with a simplified surface model. The next step will be to combine the sophisticated surface model described herein with the plasma model described in Moore (2011) and Moore et al. (2012). Other possible future work includes parametrically studying the missing portions of the frost map and the residence time of SO₂ on the non-frost surface.

Acknowledgments

This research was supported the NASA Planetary Atmospheres Grant NNG05G083G and Outer Planets Research Grant NNX08AQ49G. Computations were performed at the Texas Advanced Computing Center.

Appendix A. Supplementary material

Supplementary data associated with this article can be found, in the online version, at <http://dx.doi.org/10.1016/j.icarus.2012.05.001>.

References

- Austin, J.V., Goldstein, D.B., 2000. Rarefied gas model of Io's sublimation-driven atmosphere. *Icarus* 148, 370–383.
- Bird, G.A., 1994. *Molecular Gas Dynamics and the Direct Simulation of Gas Flows*. Oxford Univ. Press, Oxford.
- Cheng, A.F., Johnson, R.E., 1989. Effects of magnetospheric interactions on origin and evolution of atmospheres. In: Atreya, S.K., Pollack, J.B., Matthews, M.S. (Eds.), *Origin and Evolution of Planetary and Satellites Atmospheres*. University of Arizona Press, Tuscon, AZ, pp. 683–722.
- Douté, S., Schmitt, B., Lopes-Gautier, R., Carlson, R., Soderblom, L., Shirley, J. The Galileo NIMS Team, 2001. Mapping SO₂ frost on Io by the modeling of NIMS hyperspectral images. *Icarus* 149, 107–132.
- Feaga, L.M., McGrath, M., Feldman, P.D., 2009. Io's dayside SO₂ atmosphere. *Icarus* 201, 570–584.
- Gratiy, S.L., Walker, A.C., Levin, D.A., Goldstein, D.B., Varghese, P.L., Trafton, L.M., Moore, C.M., 2010. Multi-wavelength simulations of atmospheric radiation from Io with a 3-D spherical-shell backward Monte Carlo radiative transfer model. *Icarus* 207 (1), 394–408.
- Ingersoll, A.P., 1989. Io meteorology: How atmospheric pressure is controlled locally by volcanos and surface frosts. *Icarus* 81, 298–313.
- Jessup, K.L., Spencer, J.R., Ballester, G.E., Howell, R.R., Roesler, F., Vigel, M., Yelle, R., 2004. The atmospheric signature of Io's Prometheus plume and anti-jovian hemisphere: Evidence for a sublimation atmosphere. *Icarus* 169, 197–215.
- Kerton, C.R., Fanale, F.P., Salvail, J.R., 1996. The state of SO₂ on Io's surface. *J. Geophys. Res.* 101, 7555–7563.
- Linker, J.A., Kivelson, M.G., Walker, R.J., 1988. An MHD simulation of plasma flow past Io: Alfvén and slow mode perturbations. *Geophys. Res. Lett.* 15 (1), 311–314.

- Linker, J.A., Kivelson, M.G., Walker, R.J., 1991. A three-dimensional MHD simulation of plasma flow past Io. *J. Geophys. Res.* 96, 21,037–21,053.
- Marchis, F., Le Mignant, D., Chaffee, F.H., Davies, A.G., Kwok, S.H., Prangé, R., de Pater, I., Amico, P., Campbell, R., Fusco, T., Goodrich, R.W., Conrad, A., 2005. Keck AO survey of Io global volcanic activity between 2 and 5 μm . *Icarus* 176, 96–122.
- Moore, C.H., 2011. Monte Carlo Simulation of the Jovian Plasma Torus Interaction with Io's Atmosphere and the Resultant Aurora During Eclipse. PhD Dissertation, The University of Texas at Austin.
- Moore, C.H., Goldstein, D.B., Varghese, P.L., Trafton, L.M., Stewart, B., 2009. 1-D DSMC simulation of Io's atmospheric collapse and reformation during and after eclipse. *Icarus* 201, 585–597.
- Moore, C.H., Walker, A.C., Parsons, N., Goldstein, D.B., Varghese, P.L., Trafton, L.M., 2012. DSMC simulation of the plasma bombardment on Io's sublimated and sputtered atmosphere. 50th AIAA Aerospace Sciences Meeting, Nashville, TN. Jan. 9th–12th. AIAA-2012-0560.
- Moulet, A., Lellouch, E., Moreno, R., Gurwell, M.A., Moore, C., 2008. First disk-resolved millimeter observations of Io's surface and atmosphere. *Astron. Astrophys.* 482, 279–292.
- Pospieszalska, M.K., Johnson, R.E., 1996. Monte Carlo calculations of plasma ion-induced sputtering of an atmosphere: SO_2 ejected from Io. *J. Geophys. Res.* 101, 7565–7573.
- Rathbun, J.A., Spencer, J.R., Tamppari, L.K., Martin, T.Z., Barnard, L., Travis, L.D., 2004. Mapping of Io's thermal radiation by the Galileo photopolarimeter–radiometer (PPR) instrument. *Icarus* 169, 127–139.
- Sandford, S.A., Allamandola, L.J., 1993. The condensation and vaporization behavior of ices containing, SO_2 , H_2S , and CO_2 : Implications for Io. *Icarus* 106, 478–488.
- Saur, J., Strobel, D.F., 2004. Relative contributions of sublimation and volcanoes to Io's atmosphere inferred from its plasma interaction during solar eclipse. *Icarus* 171, 411–420.
- Schenk, P., Hargitai, H., Wilson, R., McEwen, A., Thomas, P., 2001. The mountains of Io: Global and geological perspectives from Voyager and Galileo. *J. Geophys. Res.* 106, 33201–33222.
- Simonelli, D.P., Dodd, C., Veverka, J., 2001. Regolith variations on Io: Implications for bolometric albedos. *J. Geophys. Res.* 106, 33241–33252.
- Sinton, W.M., Kaminski, C., 1988. Infrared observations of eclipses of Io, its thermophysical parameters, and the thermal radiation of the Loki volcano and environs. *Icarus* 75, 207–232.
- Spencer, J.R., Lebofsky, L.A., Sykes, M.V., 1989. Systematic biases in radiometric diameter determinations. *Icarus* 78, 337–354.
- Spencer, J.R., Lellouch, E., Richter, M.J., López-Valverde, M.A., Jessup, K.L., Greathouse, T.K., Flaud, J., 2005. Mid-infrared detection of large longitudinal asymmetries in Io's SO_2 atmosphere. *Icarus* 176, 283–304.
- Tsang, C.C.C., Spencer, J.R., Lellouch, E., Richter, M.J., Lopez-Valverde, M.A., Greathouse, T.K., 2012. Io's atmosphere: Constraints on sublimation support from density variations on seasonal timescales using NASA IRTF/TEXES observations from 2001 to 2010. *Icarus* 217, 277–296.
- Veeder, G.J., Matson, D.L., Johnson, T.V., Blaney, D.L., Goguen, J.D., 1994. Io's heat flow from infrared radiometry: 1983–1993. *J. Geophys. Res.* 99, 17095–17162.
- Wagman, D.D., 1979. Sublimation Pressure and Enthalpy of SO_2 . Chem. Thermodynamics Data Center, National Bureau of Standards, Washington, DC.
- Walker, A.C., Gratiy, S.L., Goldstein, D.B., Moore, C.H., Varghese, P.L., Trafton, L.M., Levin, D.A., Stewart, B.D., 2010. A comprehensive numerical simulation of Io's sublimation-driven atmosphere. *Icarus* 207, 409–432.
- Walker, A.C., Goldstein, D.B., Varghese, P.L., Trafton, L.M., Moore, C.H., 2011. Loki – A lava lake in rarefied circumplanetary cross flow. In: Levin, D., Wysong, I., Garcia, A. (Eds.), 27th International Symposium on Rarefied Gas Dynamics, 2010, AIP Conf. Proc. vol. 1333, pp. 1175–1180.